A Mid-Infrared Imaging Survey of Embedded Young Stellar Objects in the ρ Ophiuchi Cloud Core

Mary Barsony[1,2,3]

Department of Physics & Astronomy, San Francisco State University
1600 Holloway Drive, San Francisco, CA 94132

mbarsony@stars.sfsu.edu

Michael E. Ressler[2,3]

Jet Propulsion Laboratory, Mail Stop 169-327
4800 Oak Grove Drive, Pasadena, CA 91109

Michael.E.Ressler@jpl.nasa.gov

and

Kenneth A. Marsh

Jet Propulsion Laboratory, Mail Stop 168-414
4800 Oak Grove Drive, Pasadena, CA 91109

Kenneth.A.Marsh@jpl.nasa.gov

ABSTRACT

Results of a comprehensive, new, ground-based mid-infrared imaging survey of the young stellar population of the ρ Ophiuchi cloud are presented. Data were acquired at the Palomar 5-m and at the Keck 10-m telescopes with the MIRLIN and LWS instruments, at 0.5″ and 0.25″ resolutions, respectively. Of

[1]and Space Science Institute, 4750 Walnut Street, Suite 205, Boulder, CO 80301

[2]Visiting Astronomer at the W. M. Keck Observatory, which is operated as a scientific partnership among the California Institute of Technology, the University of California, and the National Aeronautics and Space Administration. The Observatory was made possible by the generous financial support of the W. M. Keck Foundation.

[3]Observations with the Palomar 5 m telescope were obtained under a collaborative agreement between Palomar Observatory and the Jet Propulsion Laboratory.

172 survey objects, 85 were detected. Among the 22 multiple systems observed, 15 were resolved and their individual component fluxes determined. A plot of the frequency distribution of the detected objects with SED spectral slope shows that YSOs spend $\sim 4 \times 10^5$ yr in the Flat Spectrum phase, clearing out their remnant infall envelopes. Mid-infrared variability is found among a significant fraction of the surveyed objects and is found to occur for all SED classes with optically thick disks. Large amplitude near-infrared variability, also found for all SED classes with optically thick disks, seems to occur with somewhat higher frequency at the earlier evolutionary stages. Although a general trend of mid-infrared excess and NIR veiling exists progressing through SED classes, with Class I objects generally exhibiting $r_K \geq 1$, Flat Spectrum objects with $r_K \geq 0.58$, and Class III objects with $r_K = 0$, Class II objects exhibit the widest range of r_K values, ranging from $0 \leq r_K \leq 4.5$. However, the highly variable value of veiling that a single source can exhibit in any of the SED classes in which active disk accretion can take place is striking, and is direct observational evidence for highly time-variable accretion activity in disks. Finally, by comparing mid-infrared vs. near-infrared excesses in a subsample with well-determined effective temperatures and extinction values, disk clearing mechanisms are explored. The results are consistent with disk clearing proceeding from the inside-out.

Subject headings: ISM: individual objects: ρ Ophiuchi cloud—planetary systems: protoplanetary disks—stars: formation — stars: pre-main-sequence — surveys

1. Introduction

The ρ Ophiuchi cloud core continues to be the subject of intense study at all wavelengths, since it harbors the nearest site of the formation of several hundred young stellar objects (YSOs). Mid-infrared observations of $\sim$ 2 dozen YSOs in the ρ Oph cloud core resulted in the development of the currently accepted classification scheme for such objects (Lada & Wilking 1984; Lada 1987). The most comprehensive previous ground-based mid-infrared survey of the ρ Oph clouds included 56 objects, 49 of which were in the central L1688 cloud core (Greene et al. 1994). A survey of the entire YSO population of the ρ Oph cloud core became practicable for the first time with the advent of mid-infrared arrays mounted on large-aperture ground-based telescopes towards the end of the last decade. It is just such a survey that is the subject of this work.

Mid-infrared studies of YSOs are especially relevant for studies of young, planet-forming

disks, since mid-IR emission peaks at distances of order $\sim$ 1 AU from the central object. By contrast, near-infrared continuum (NIR) emission from hot dust originates closer to the central YSO (Eisner et al. 2003; Millan-Gabet et al. 2001; Millan-Gabet et al. 1999). Comparison of the near- and mid-infrared properties of young disks is useful for understanding disk structures (Chiang & Goldreich 1997), whereas multi-epoch comparison of mid-infrared fluxes with previous (Bontemps et al. 2001) and future (Spitzer Legacy and GTO) observations will aid our understanding of disk accretion processes.

Of obvious importance for planet formation are not only studies of average YSO disk lifetimes e.g., (Haisch et al. 2001), but also studies of disk dissipation processes (Armitage et al. 2003). Comparative studies of the population of very young ($\leq$ 1 MYr), diskless YSOs (Wilking et al. 2001) with the equally young population of YSOs with optically thick disks detected in the present survey, should greatly aid our understanding of the reason for the observed widely varying disk dissipation timescales.

Finally, no current space-based observatory can match the angular resolution achievable from the ground at mid-infrared wavelengths, which is ideal for studying young binaries and their disks at the distance to the ρ Oph clouds. Since the majority of young stars form in binary/multiple systems, studies of planet-forming disks must, of necessity, include studies of the disks in multiple systems. The binary separation of YSOs at the distance to the ρ Oph clouds peaks near a projected angular separation of $0.25''$ (Barsony et al. 2003), which is the diffraction-limit of the Keck 10-meter telescopes at 10 μm.

In the following, we describe the source selection criteria for our mid-infrared survey, along with the data acquisition and data reduction procedures in § 2. The key results of our new, mid-infrared survey are presented in § 3 and the implications of these are discussed in § 4.

2. Source Selection Criteria, Observations, and Data Reduction

The starting point for our target list was the near-infrared imaging survey (Barsony et al. 1997) of the central square degree of the ρ Ophiuchi cloud core (also known as L1688), which catalogs 4495 objects. To winnow this source list to a manageable number of target objects, while maximizing the likelihoods of cloud membership and of mid-IR detectability, we imposed combined near-infrared brightness and color criteria. Target objects for this study were, therefore, required to be bright at 2.2 μm (K$\leq$13.0), since YSOs are generally bright NIR emitters, even when highly reddened, and had to have very red NIR color (H$-$K $\geq$ 1.67), since high near-infrared excess is generally a disk indicator.

Since ρ Oph is, for the most part, a low-mass star-forming cloud, at its distance of 140 pc, the apparent magnitude range $5 \leq K \leq 10.5$ essentially encompasses its entire population, not allowing for extinction. According to theoretical pre-main-sequence isochrones, one million year old YSOs at the hydrogen-burning limit of ≈ 0.08 $M_{\odot}$ should have an apparent $K = 10.5$ at this distance, with no foreground extinction (Wilking et al. 1999). At the other end of the mass spectrum, a similarly youthful Herbig Ae star of 4 $M_{\odot}$, WL16, is observed to have an apparent $K = 7.92$ in ρ Oph, seen through $A_V = 31$ (Ressler & Barsony 2003).

Using the relation $A_K = 1.4(H - K)$, our color selection criterion of $H - K \geq 1.67$, would result in $A_K \geq 2.3$, assuming an intrinsic $(H - K)_0 = 0.0$ (Cohen et al. 1981). Using the relation, $A_V = 15.4 \times [(H - K)_{obs} - (H - K)_0]$, and noting that $(H - K)_0 = 0.3$ for an M dwarf with no infrared excess, our color selection criterion of $H - K \geq 1.67$, when combined with our apparent brightness criterion of $K \leq 13$, guarantees that we are sampling the cloud core's embedded population through $A_V \sim 21$ even for young brown dwarfs. At the other end of the brightness scale, these selection criteria could also include occasional stray background K and M giants out to ~ 1 kpc, depending on the actual obscuration along the line-of-sight. In fact, the most recent NIR spectroscopic survey of the ρ Ophiuchi YSO population has shown that of the 80 objects in common to both surveys, only six of our target list (Elias 35, GY232, VSSG6, GY65, GY45, BKLT J162618−242818) are confirmed background K or M giants (Luhman & Rieke 1999).

The combined color and brightness criteria described above, when applied to the BKLT survey, selected 104 of 4495 objects, of which all but 7 (GY12, GY30, IRS 26, BKLT 162805−243354, GY 312, BKLT 162629−241748, and BKLT 162735−244628) were observed by us in the mid-infrared. This source list was supplemented with objects that were known or suspected to be cloud members from various optical emission-line, near-infrared, and far-infrared surveys, but which did not satisfy the above-mentioned combined color and brightness criteria (Struve & Rudkjøbing 1949; Dolidze & Arakelyan 1959; Vrba et al. 1975; Elias 1978; Wilking & Lada 1983; Young et al. 1986; Wilking et al. 1989; Leous et al. 1991; Greene & Young 1992; Barsony et al. 1997; Comeron et al. 1993). In total, we report mid-infrared fluxes or flux upper limits for 172 individual objects. The spatial distribution of the objects targeted by this survey is plotted in Figure 1, overlaid on the contours of $C^{18}O$ (J=2→1) emission from the cloud core, for reference (Wilking & Lada 1983).

The mid-infrared imaging data for this survey of the ρ Oph cloud core's embedded population were obtained with MIRLIN, JPL's 128 × 128 pixel Si:As camera (Ressler et al. 1994), and the University of California's Long Wavelength Spectrometer (LWS) (Jones & Puetter 1993). The relevant observing and data reduction parameters are listed in Table 1. The first column lists the UT date of observation, the second column specifies the telescope used. All

observations at Palomar and on Keck II were made with MIRLIN, whereas LWS was the instrument used on Keck I.

The MIRLIN data were acquired at N-band ($\lambda_0 = 10.78$ μm, $\Delta\lambda = 5.7$ μm). However, in order to avoid saturating the medium-well-depth Si:As detector of the LWS instrument, a narrower band, 12.5 μm filter ($\lambda_0 = 12.5$ μm, $\Delta\lambda = 1.0$ μm) was used. MIRLIN has a plate-scale of 0.138″/pixel and a 17.7″ × 17.7″ field of view at the Keck II telescope; corresponding values for MIRLIN at the Palomar 5-meter are 0.15″/pixel and 19.2″ × 19.2″, respectively. At the Keck I telescope, the LWS instrument has a plate-scale of 0.08 ″/pixel and a 10.2″ × 10.2″ field-of-view. For reference, the full-width at half-maximum of a diffraction-limited image at N band is $\sim 0.25''$ at the Keck Telescopes and 0.47″ at the Palomar 5-meter.

Data were acquired with traditional mid-IR chopping and nodding techniques. Specifically, for MIRLIN observations, the telescope's secondary mirror was chopped 8″ in a north-south direction, at a rate of a few Hz; then the entire telescope was nodded 8″ east-west, in order to remove residual differences in the background level. Total on-source integration times were typically 24-25 seconds at each telescope for the program sources. On-source integration times consisted of several hundred to a thousand coadded chop pairs, with 5-6 msec integration times per frame. For the LWS observations, the secondary mirror chop throw was 4″, as was the telescope nod, 4″ alternately on either side of the source along a straight line. The LWS chop frequency was 4.8 Hz, integration times per frame were 15 msec, and typical total on-source integration times were 72 seconds. All raw images were background-subtracted, shifted, and co-added with our in-house IDL routine, "mac" (match-and-combine).

The flux standards observed for each night are listed in Column 3 of Table 1, along with corresponding N band magnitudes in Column 4. These were also used for airmass monitoring. Photometry for the standard stars was performed in circular software apertures with radii (in arcsecond units) indicated in Column 5 of Table 1. A straight-line fit to the instrumental minus true magnitudes of the standards as a function of airmass for each night resulted in the determination of the airmass corrections and zero-point offsets listed in Columns 8 and 9 of Table 1, respectively. No airmass corrections were used for the Keck data, whereas typical airmass corrections at Palomar were of order 0.1−0.2 mags/airmass. Photometric consistency between all standards during a given night's observing was typically of order ± 0.05 magnitudes. By adding the errors in the zero-point offsets, the airmass corrections, the aperture corrections, and the uncertainties in the magnitudes of the standards in quadrature and taking the square root, we estimate the total photometric accuracy of the Keck data to be good to ± 0.06 magnitudes, and the Palomar data to ± 0.08 magnitudes. To convert these errors to Janskys, note that 0.00 magnitudes at N-band with MIRLIN corresponds to

33.4 Jy, whereas 0.00 magnitudes at 12.5μm with LWS corresponds to 25.2 Jy.

Photometry for program sources was typically performed in the software apertures listed in Column 6 of Table 1, under the column heading, "Target Object Aperture Radius." Aperture corrections were derived from the flux standards for each night, and applied to each target object's instrumental magnitude before application of the zero-point calibration and airmass correction. The aperture corrections for each night's observing are listed in Column 7 of Table 1. For bright sources with N $\leq$ 3.5, the same software apertures were used as for the bright standards. For the case of sources so extended that they appear significantly brighter in a larger software aperture, a software aperture large enough to include all of the detected flux was used.

In the case of close companions, the combined system flux was first determined from a software aperture chosen to be large enough to contain both objects. Subsequently, the relative photometry of each component was determined by fitting a known point-source calibrator (generally one of the flux calibrators observed that night) to the individual source peaks. The total flux was then divided amongst the components in the ratio determined by the relative point-source fitting photometry.

Upper limits were calculated in the same apertures as faint target objects. The resultant background subtracted counts/sec were multiplied by a factor of three, and the result converted to Jy units. Averaging the upper limits obtained in this manner for each telescope/instrument combination, it is found that the mean 1 σ flux errors were 0.018 $\pm$ 0.024 Jy at 12.5 μm with LWS at Keck I, 0.008 $\pm$ 0.005 Jy at 10.8 μm with MIRLIN at Keck II, and 0.029 $\pm$ 0.033 Jy at 10.8 μm with MIRLIN at Palomar.

3. Results

The mid-infrared photometry for our target objects is presented in Table 2. The list is R.A. ordered. The first column of Table 2 lists the BKLT source name, and the third and fourth columns list the objects' J2000 coordinates from Barsony et al. 1997. For reference, the second column of Table 2 lists a common, alternative alias for each BKLT object (for cross-references of aliases for infrared sources, see Barsony et al. 1997). The fifth and sixth columns list each object's mid-infrared flux or flux upper limit in Jy units (either at 10.8 μm for MIRLIN data, or at 12.5 μm for LWS data). The seventh column lists the UT date of observation, and the eighth and last column lists the telescope/instrument combination used. In some cases, several entries exist for the same object, if it was observed on more than one occasion. In such instances, the different measurements are separately tabulated.

In Figures 2 & 3, we compare our results with *ISOCAM* photometry (Bontemps et al. 2001). These authors list photometry for 212 objects, of which 199 are in the L1688 cloud core, and the rest are in L1689. There are 120 members of L1688 common to both surveys. Figure 2 is a plot of detected objects from Table 2 that are in common with *ISOCAM*-detected objects. Figure 3 is a plot of sources with upper limits listed in Table 2 that are in common with *ISOCAM*-detected objects.

In Figure 2, we compare our ground-based mid-infrared photometry for 69 sources that were detected in both *ISOCAM* filters. The published *ISOCAM* fluxes are for filters centered at 6.7 μm and 14.3 μm. For comparison with MIRLIN data, whose broadband N filter is centered at 10.8 μm, we linearly interpolated the published *ISOCAM* fluxes to 10.8 μm. These objects are represented by filled diamonds in Figure 2. For comparison with LWS data, whose narrower filter was centered at 12.5 μm, we linearly interpolated the published *ISOCAM* fluxes to 12.5 μm. These objects are represented by the filled squares in Figure 2. The straight line plotted in Figure 2 represents perfect agreement between the measurements reported in this survey and the interpolated measurements from *ISOCAM*. The agreement is generally good between the two datasets. This means that the ground-based fluxes agree with the *ISOCAM* fluxes to within 3σ of the published uncertainties. For the sources with good agreement between the ground-based and *ISOCAM* fluxes, we can infer that any extended emission on scales $\leq 18''$ is below our detection limit, since $18''$ diameter apertures were used for the *ISOCAM* flux measurements (except for the faintest sources, for which a $9''$ diameter aperture was used), whereas a much smaller software aperture was used for the ground-based flux measurements (see Table 1). Sources whose measured fluxes have larger discrepancies between the ground-based and *ISOCAM* values are either intrinsically variable or have significant extended emission. These are listed in Table 3 and discussed in § 4.2.

Four objects in common to both surveys, BKLT J162609−243411 (SR-3) , BKLT J162634−242330 (S1), BKLT J162702−243726 (WL16), and BKLT J162659−243458 (WL22), do not have *ISOCAM* fluxes available, although they are strong mid-infrared emitters. All four are inferred to be embedded early-type stars associated with extended mid-infrared emission (Bontemps et al. 2001). For SR-3, a star of spectral type A0 (Struve & Rudkjøbing 1949), we find a 10.8 μm flux of 0.15 Jy (see Table 2), whereas its previously published N-band flux, observed through a $6''$ or $8''$ aperture, was 0.36 Jy (Lada & Wilking 1984). These findings are consistent with the presence of extended mid-infrared emission for this source. For S1, a star of B4 spectral type (Bouvier & Appenzeller 1992), we find a 10.8 μm flux of 0.065 Jy, corresponding to N=6.77 (see Table 2). Previous ground-based mid-infrared photometry for this object was 4.9 magnitudes at 11.1 μm in an unspecified, but presumably larger, aperture (Vrba et al. 1975), consistent with the presence of extended mid-IR emission centered on S1. This object is listed as displaying a double-peaked spectral energy distribution by Wilking

et al. (2001). A detailed, spatially-resolved study of the embedded Herbig Ae star, WL16, shows that the extended mid-infrared emission from this source originates from a $\sim$ 900 AU diameter inclined disk composed of PAH (polycyclic aromatic hydrocarbon) and VSG (very small grain) particles, obscured by a foreground extinction of $A_V = 31$ magnitudes (Ressler & Barsony 2003). WL22 is inferred to be of early spectral type due to its relatively high infrared luminosity, strong, extended, mid-infrared emission, and lack of millimeter continuum flux.

Figure 3 is a plot of the objects common to both surveys, for which only upper limits are available from the ground-based observations reported here. Filled-diamond symbols indicate 10.8 μm flux upper limits derived from MIRLIN observations; filled squares indicate 12.5 μm flux upper limits derived from LWS observations. Downward pointing arrows represent the *ISOCAM* upper limits. Again, the published *ISOCAM* fluxes are for filters centered at 6.7 μm and 14.3 μm. For cases where both 6.7 μm and 14.3 μm *ISOCAM* fluxes are available, we have linearly interpolated the *ISOCAM* fluxes to 10.8 μm for direct comparison with the MIRLIN data (filled diamonds) and to 12.5 μm, for direct comparison with the LWS data (filled squares). For those cases where only 6.7 μm *ISOCAM* fluxes were available, we have taken the quoted 15 mJy completeness limit at 14.3 μm as if it were the actually measured 14.3 μm flux, to derive strict interpolated *ISOCAM* upper limits at 10.8 μm and 12.5 μm for comparison with the ground-based upper limits. In Figure 3, the straight line is a locus of points representing perfect agreement between ground-based photometry and the interpolated *ISOCAM* fluxes. Only one object, GY 301, has an inferred 10.8 μm *ISOCAM* flux that differs significantly from the ground-based measurement at this wavelength.

There remain 78 members of the L1688 cloud core for which only *ISOCAM* photometry is available. Of these, only 3 met this survey's primary selection criteria of $K \leq 13.0$ and $H - K \geq 1.67$. These three objects (GY 12, IRS 26, and GY 312) are a subset of the 7 objects listed in §2 which met our selection criteria, but were unobserved by us. Conversely, there are 4 sources meeting our selection criteria and not observed by us, which fell within the areas of L1688 surveyed by *ISOCAM*, but which are not listed among the 199 L1688 cloud members. These objects are GY30, BKLT 162629-241748, BKLT 162735-244628, and BKLT 162805-243354. It is likely that the first 3 of these have mid-infrared colors of background objects, and were excluded from membership in the L1688 cloud on that basis. Note, however, that GY 30 has recently been discovered to drive a molecular outflow, and illuminates a fan-shaped reflection nebulosity (Kamazaki et al. 2003; Dent et al. 1995). The source, BKLT 162805-243354, just 4″ South of GY 472, may not have been resolved with *ISOCAM*. In summary, all of the objects meeting our selection criteria, but unobserved by us, merit further investigation.

Finally, 41 objects in Table 2, of which 37 fell within the ISOCAM survey's field of view, are not listed among the L1688 cloud members observed by ISOCAM. The fact that only flux upper limits were measured from the ground-based observations reported here for 34 of 37 of these objects, is consistent with their being background sources. The three exceptions are GY263, GY232, and BKLT162618-242818, for which there are ground-based detections (see Table 2), but no ISOCAM fluxes are published. Two of these, GY232 and BKLT162618−242818, have been spectroscopically determined to be background giants (Luhman & Rieke 1999). The nature of GY263 remains to be determined. There are 4 objects in this ground-based survey which fell outside of the *ISOCAM* survey's field-of-view: WLY64=IRAS64a, SR-2, BKLT162904-244057, and BKLT162522-243452. WLY64 exhibits an M8-M9 III optical spectral type, but a K4 III NIR CO-band absorption, very similar to FU Ori objects (Luhman & Rieke 1999). SR-2 has a G8 spectral type and had been assumed to be a foreground object based on its NIR colors (Elias 1978). More recent, high-dispersion, optical spectroscopy has shown SR-2 to be a pre-main-sequence member of the ρ Oph cloud core, however (Walter et al. 1994). The nature of the other two objects remains to be determined.

4. Discussion

4.1. Relative Timescales within SED Classes: The Flat Spectrum Objects

For nearly two decades now, young stellar objects have been age-ordered according to an empirical classification scheme based on the slope, a, of their near-infrared (2.2 μm) to mid-infrared (10 μm) spectral energy distributions (SEDs) :

$$a \;=\; \frac{d\log\left(\lambda F_\lambda\right)}{d\log\lambda}.$$

In this scheme, Class I SEDs have $a \geq 0.3$, Flat Spectrum SEDs have $-0.3 \leq a \leq +0.3$, Class II SEDs have $-0.3 \geq a \geq -1.6$, and Class III SEDs have $a \leq -1.6$ (Greene et al. 1994). These latter authors were the first to suggest that the Flat Spectrum SEDs be identified as a distinct class, since YSO's with $+0.3 \geq a \geq -0.3$ were found to have spectra strongly veiled by continuum emission from hot, circumstellar dust, unlike the case for the near-infrared spectra of typical, classical T-Tauri stars (those generally associated with Class II SEDs).

In general, the above spectral slope classes have been found to correspond to distinct physical objects, defined by the amount and geometry of the circumstellar material surrounding the central, forming YSO. Thus, a Class I object is one in which the central YSO has essentially attained its initial main-sequence mass, but is still surrounded by a remnant

infall envelope and accretion disk; a Class II object is surrounded by an accretion disk; and a Class III object has only a remnant, or absent, accretion disk. The gradual clearing of circumstellar matter has been interpreted as an evolutionary sequence.

In this context, in most cases the SED class reflects the evolutionary state. As a cautionary note, however, there may be instances in which the SED class does not give the correct evolutionary state. For instance, a T-Tauri star seen through a great amount of foreground obscuration may display a Class I or Flat Spectrum SED (since the 2 μm flux suffers heavier extinction that the 10 μm flux). Additionally, orientation effects can also be very important, since a more pole-on Class I object may have an SED similar to an edge-on Class II object (Whitney et al. 2003). The definitive way to ascertain the evolutionary state of a YSO is to obtain resolved images of the given object at several different infrared wavelengths, and to compare these images quantitatively with model images produced using 3-D radiative transfer codes (Whitney et al. 2003). Since such data are unavailable for our current source sample, our analysis of the current dataset, in terms of ascertaining the relative number of objects in each evolutionary state, is necessarily limited to a plot of the distribution of spectral slope values, a.

Figure 4 shows histograms of the near- to mid-infrared spectral slope distributions for the young stellar population of the ρ Ophiuchi cloud core. The solid line shows the spectral slope distribution determined for the objects in our ground-based study. The spectral slopes, a, were determined using the near-infrared (2.2 μm) photometry of BKLT and the mid-infrared photometry presented in Table 2 (at 10.8 μm for MIRLIN data and at 12.5 μm for the LWS data). The dashed line shows the spectral slope distribution of objects from the *ISOCAM* study. Spectral slopes, a, in this case were determined from the 2.2 μm photometry of BKLT and the 14.3 μm photometry from *ISOCAM* (Bontemps et al. 2001).

It is striking that there are more objects exhibiting Flat Spectrum near- to mid-infrared spectral slopes, a, than Class I spectral slopes in Figure 4. The number of sources exhibiting Flat Spectrum slopes is about 1/2 the number exhibiting Class II spectral slopes. This result holds for both the ground-based (solid line) the *ISOCAM* (dashed line) histograms.

Recent two-dimensional radiative transfer modelling has shown that the SEDs of Flat Spectrum objects are reproduced by a central star + disk system embedded in a relatively tenuous halo (Kikuchi et al. 2002). The dusty halo in Flat Spectrum objects is what is left of the remnant infall envelope with cavities carved out by outflows seen in the Class I objects. The dusty halo of Flat Spectrum objects serves to heat the disk by scattering and reprocessing the central PMS star's radiation. It is the photosphere of the warmed disk that is responsible for the large mid- to far-infrared excesses that produce the observed flat spectral slope observed in these objects.

The reason previous authors have neglected to remark upon the large fraction of sources exhibiting Flat Spectrum slopes in the ρ Oph cloud is because they had de-reddened the spectral slopes assuming these objects had intrinsic colors of T-Tauri stars (Bontemps et al. 2001, Wilking et al. 2001). Such a procedure relies on the assumption that the observed source is a Class II object, seen through high foreground extinction. However, in the presence of heated and reprocessing halos, such as are present in the Flat Spectrum phase, such a dereddening procedure is problematic. Complications due to heating and re-processing of both stellar and disk radiation in the remnant infall envelopes also preclude the "de-reddening" of Class I objects.

The important result here is that there is a non-negligible phase in YSO evolution marking the transition between the Class I and Class II or Class I and young Class III phases. During this reasonably lengthy transitional, or Flat Spectrum phase, a dusty halo remnant envelope remains and is slowly dispersed. Of the sources in our survey that could be assigned to SED classes based on our data, there are 19 Class I, 23 Flat Spectrum, 37 Class II, and 21 Class III objects. The *ISOCAM* data from Tables 2-5 of Bontemps et al. (2001) contain 20 Class I, 30 Flat Spectrum, 78 Class II, and 19 Class III objects (note, however, that the *ISOCAM* SED slopes are derived from 2–14 μm). Flat Spectrum objects make up 23% and 20% of the total number of classified objects in each survey, respectively. The ratio of Flat Spectrum to Class I objects is 1.2 in our survey and 1.5 in the *ISOCAM* survey. The typical lifetime of an object in the Flat Spectrum phase is comparable (or perhaps slightly greater than) that in the Class I phase. For a solar-luminosity object, this would correspond to 4 x 10^5 yr based on the study of Wilking et al. (1989).

4.2. Active Accretion and Variability at Mid-Infrared Wavelengths

Table 3 lists the objects whose fluxes, as measured in this survey, differ significantly from their published *ISOCAM* fluxes, or from other previously published ground-based mid-infrared photometry. Sources are included in Table 3 if the difference between two flux measurements exceeds the quoted 3-σ errors. To compile this table, we have included previously published mid-infrared photometry, in addition to the fluxes plotted in Figures 2 & 3 (Wilking et al. 2001; Greene et al. 1994; Wilking et al. 1989; Lada & Wilking 1984; Rydgren et al. 1976). In Table 3, the first column lists the BKLT source designation, and the second column lists a more common alias. The 10.8 μm flux and its associated error measured with MIRLIN are listed in the third colum. For direct comparison, the interpolated 10.8 μm flux and its associated error from the *ISOCAM* data are listed in the fourth column. The 12.5 μm fluxes measured with LWS are next listed in the fifth column, and

the interpolated 12.5 μm fluxes and their associated errors from *ISOCAM* are listed in the sixth column. Finally, the last column lists previous ground-based mid-infrared photometry. These latter fluxes are all at 10.2 μm, except for WL17, whose 12.5 μm flux is listed.

The source of the flux discrepancies in Table 3 can either be intrinsic source variability or the presence of extended emission. Intrinsically variable sources in Table 3 are those for which fluxes from this survey exceed measured fluxes from previous surveys (all of which used larger apertures). For sources whose previous flux measurements, taken in larger apertures, exceed the fluxes from this survey, further high-resolution photometry is required to distinguish between source variability and the presence of significant extended emission. These sources are, nevertheless, included in Table 3 as possibly variable sources.

Figure 5 shows the SED slope distribution of the mid-infrared variables and candidate variables of Table 3. Clearly, mid-infrared variability occurs for all SED classes with optically thick disks. We have also plotted in Figure 5 the SED slope distribution of known near-infrared variables in ρ Oph from Table 5 of Barsony et al. (1997). Near-infrared variability, also found for all SED classes with optically thick disks, seems to occur with somewhat higher frequency at the earlier evolutionary stages (Flat Spectrum and Class I). Whereas 89% of NIR variables are in the Class I or Flat Spectrum stage, only 56% of the mid-IR variables are. This tendency must be verified from future sytematic NIR and mid-IR variability studies to improve the statistics.

Sources exhibiting variability at both near- and mid-infrared wavelengths are WL12, WL17, WL19, GY244, GY245, GY262, and IRS44. WL15, an almost face-on Class I object, appears variable at near-, but not at mid-infrared wavelengths. The rest of the mid-infrared variables listed in Table 3 are apparently not highly variable at near-infrared wavelengths. However, further systematic variability studies in the infrared are needed to verify these preliminary results.

In order to understand what distinguishes the population of mid-infrared variables from the rest of the embedded population in ρ Oph, we use the data compiled in Table 4 to look for a correlation between mid-infrared variability and presence of an active accretion disk, as signalled by near-infrared veiling. The r_K values tabulated in Table 4 are all *spectroscopically* determined, and are, therefore, reddening-independent. By using moderate ($R \sim 2000$) to high ($R \sim 20000$) resolution near-infrared spectroscopy, one can deduce the $K-$band "veiling" of photospheric absorption lines in a YSO by comparison with the shapes of the same absorption lines found in a spectroscopic standard star of the same spectral type. One then varies the "veiling" applied to the standard star's spectrum until the "veiled" standard star's spectrum best matches the YSO's spectrum. Such a "veiling" measurement is independent of reddening, given the narrow wavelength range in which the relevant spectral

lines lie.

The objects in Table 4 are listed in reverse near- to mid-infrared spectral slope (a) order, from the largest values, corresponding to Class I objects, to the smallest values, corresponding to Class III objects. The spectral slopes in Table 4 were deterrnined using the near-infrared (K-band, or 2.2 μm) photometry of BKLT and either the 10.8 μm flux from MIRLIN, or the 12.5 μm flux from LWS, as available, and as listed in Table 2.

We have excluded the known background giants from the entries in Table 4. Also excluded are the two known PAH/VSG emitters, WL16 and WL22. Table 4 lists the BKLT source designation in the first column and an alternate alias for each source in the second column. The K magnitude and H−K color for each object are listed in the third and fourth columns, respectively, and are taken from Barsony et al. (1997), except for the following: WL20, GSS30 IRS3 (Strom et al. 1995), GY197 (Comeron et al. 1993), WL1 (Haisch et al. 2002), WL18, Elias 26 (Haisch 2003), and DoAr24E (Chelli et al. 1988). Each object's spectral slope, a, between 2.2 μm and either 10.8 μm or 12.5 μm (as available from Table 2), and corresponding SED class, are listed in the fifth and sixth columns respectively. Published, spectroscopically-determined, K-band veiling values, and visual extinctions are listed in the seventh and last columns, respectively.

Continuum veiling at K (2.2 μm) is quantified by the value, r_K, defined as F_{excess}/F_K, where F_K is the intrinsic photospheric flux of the central object at K, and F_{excess} is the amount of observed K-band flux in excess of the expected photospheric value. Veilings of $r_K \geq 0.5$ have been attributed to the presence of actively accreting circumstellar disks (Luhman & Rieke 1999; Wilking et al. 2001). Figure 6 presents a graph of the near- to mid-infrared spectral slopes, a, from Table 4, plotted against the *spectroscopically determined* r_K values published by various authors (Greene & Meyer 1995; Wilking et al. 1999; Luhman & Rieke 1999; Barsony et al. 2002; Greene & Lada 2002; Prato et al. 2003; Doppmann et al. 2003; Doppmann 2004). The horizontal dashed line in Figure 6 denotes the boundary between optically thick (above the line) and optically thin (below the line) disks, at $r_K = 0.58$ (Wilking et al. 2001). Class I objects generally exhibit $r_K \geq 1$ (the one exception being GY91/CRBR42 with $r_K = 0.3$). Flat Spectrum objects generally have $r_K \geq 0.58$ (with the exception of GY244, with $r_K = 0$). Class II objects have the widest range of r_K values, ranging from $0 \leq r_K \leq 4.5$ (the record of 4.5 being held by Elias 26). Class III objects, clearly have optically thin disks, most with $r_K = 0$. The most striking feature of this graph is the highly variable value of veiling that a single source can exhibit in any of the SED classes in which active disk accretion can take place (*i.e.*, in the Class II/Flat Spectrum/Class I phases). This is direct observational evidence for highly time-variable accretion activity in disks.

4.3. Disk Structures

A current problem of great interest is how disks are dissipated in YSOs. Is it possible that disk winds would preferentially clear the innermost portions of a disk before the outer portions, or vice versa? One possible way to address this question is to look for the frequency of near-infrared vs. mid-infrared excesses, perhaps as a function of the age of the system, since near-IR excesses originate from disk regions much closer to the central object than mid-IR excesses.

For this purpose, we will consider only those Class II and Class III objects whose effective temperatures have been spectroscopically determined, and that have good estimates of A_V. We have omitted the known binaries, S1, SR24N, WL13, Elias 34, IRS2, and GSS29 (Barsony et al. 2003; Doppmann 2004) from this plot. These systems would either be unresolved by our mid-infrared data (spectroscopic binaries) or their projected angular separations are so small that both of their spectra would fall into a single slit, thereby invalidating the derived effective temperature and visual extinction values. Individual components of well-resolved multiple systems have been included in Figure 7, however.

We calculate K-band excesses, ΔK, and N-band excesses, ΔN, defined as the logarithm of the ratio of the observed flux to the flux expected from the PMS star's photosphere at 2.2 μm and 10.8 μm, respectively, seen through the appropriate amount of foreground extinction. More specifically, we use the definitions, $\Delta K = logF(observed)_{2.2\mu m}/F(photospheric)_{2.2\mu m}$ (Strom et al. 1989), and $\Delta N = logF(observed)_{10.8\mu m}/F(photospheric)_{10.8\mu m}$ (Skrutskie et al. 1990). Note that this method of calculating r_K is reddening dependent, since it results in a different ΔK value for a different input A_V, in contrast to the spectroscopically determined values of r_K used in Figure 6.

Figure 7 shows the resulting ΔN vs. ΔK plot. In the left panel, the expected photospheric contributions at K and N were determined assuming a blackbody radiator at the spectroscopically determined effective temperature for each source. In the right panel, Kurucz model atmospheres of the appropriate temperature, with solar abundances, and $log\ g = 3.5$, were used to infer the photospheric emissions at K and N. Class III objects are plotted as triangles, and Class II objects as squares. The demarcations between opticallly thin/thick disks at ΔK =0.2 and at ΔN =1.2 are indicated by the dashed and dotted lines, respectively (Skrutskie et al. 1990).

Class III objects, as expected, have optically thin disks at both near- and mid-infrared wavelengths, with ΔK values scattered about 0.0 (for the blackbody models). There is an inherent bias in the sample of Class III objects plotted in Figure 7, since in order to appear on this plot, they are all detected in the mid-infrared. Therefore, instead of being scattered

about a mean $\Delta N = 0.0$, there appears to be a positive bias in the ΔN values of these Class III objects.

The sample of Class III objects plotted here are unique in that they have any detectable mid-infrared emission above photospheric at all, signalling the presence of surrounding disks, even though these are opticallly thin. These seem to have been cleared possibly from inside out (Δ K consistent with photospheric emission only, but Δ N above photospheric).

The dramatic finding in Figure 7 is the lack of any objects occupying the lower right quadrant of each plot, corresponding to optically thick inner disks with optically thin outer disks, for both the blackbody and Kurucz model central objects. This finding is consistent with two possible disk dissipation scenarios: either disk clearing proceeding at the same rate at all radii or disk clearing from the inside-out. For the case of disk clearing proceeding at the same rate at all radii, we would expect to see a clear correlation between Δ K and Δ N, whereas for disk clearing from the inside-out, we would expect all of the quadrants of Figure 7, except the lower right, to be significantly populated.

At first sight, it may seem as though there is a correlation between Δ K and Δ N, in the left-panel of Figure 7, with the exception of GY11. However, the sources, GY314, GSS29, GSS39 have been previously pointed out as examples of disks with inner holes (Wilking et al. 2001), which should occupy the upper left quadrant in each panel of Figure 7. In fact, GY314 does lie in the upper left quadrant of each panel of Figure 7, whereas GSS 39 lies no further than Δ N= 0.1 from this quadrant even in the case of a blackbody model for the central object (GSS29 is a newly discovered spectroscopic binary, and has been excluded from Figure 7 on that basis). If we allow an error of just Δ N =0.1 in the mid-IR excess determinations for the blackbody models, then the upper two quadrants for both central source models would be equally occupied, and one could argue for evidence for disk clearing from the inside-out.

Of course, were we to consider only the right panel, where Kurucz model atmospheres have been used to model the central objects, we would conclude that disk clearing does proceed from the inside out. However, we must point out a systematic error that seems to be present in the near-infrared excesses as determined when using Kurucz model atmospheres for the central objects: Instead of being equally distributed about a Δ K = 0 value, as would be expected for random errors for lack of NIR excess emission, the objects with optically thin disks are scattered about a mean negative value of Δ K = -0.1. This systematic error could be caused by the presence of just 10%–20% veiling at J band, or by the presence of some scattered light at J.

To definitively decide on the disk clearing mechanism, two avenues of further investi-

gations are called for. First, spectral type determinations for more Class II and Class III sources are needed, in particular, ones for which the K and N band fluxes are known, in order to improve the statistics of Figure 7. Secondly, detailed investigations of the contributions to each individual object's J band flux from scattering and/or veiling are needed, in order to more accurately determine the K band excesses when using Kurucz model atmospheres.

4.4. Effect of Multiplicity on Disk Evolution

Table 5 lists the targets observed in our mid-infrared survey that are known to be in multiple systems (Barsony, Koresko, & Matthews 2003). Of a total of 22 multiple systems observed, two were new discoveries: IRS 34, at 0.31″ separation, and WL1 at 0.82″ separation. Fifteen of the observed, known multiple systems were resolved in this study. Individual component fluxes and/or flux upper limits are listed in Table 5.

Data from this survey have been used to study the multiplicity frequency among Class I protostars, with the result that the restricted companion fraction for the observed magnitude difference and separation range is consistent with that found for Class II objects. Thus, the restricted companion fraction for both Class I and Class II objects exceeds that found for main-sequence stars by a factor of two (Haisch et al. 2002; Haisch et al. 2004). These authors also inferred that many sub-arcsecond Class I binaries remain to be discovered.

The question of how binarity affects disk evolution may be divided into several categories, based on binary separation (Looney et al. 2000). Gravitationally bound objects evolving from separate envelopes ($\geq$ 6500 AU separation), objects with separate disks, but common envelopes (100 AU $\leq$ r $\leq$ 6500 AU), and objects sharing both a single disk and a single envelope ($\leq$ 100 AU separation) must evolve differently. The angular scales accessible in this survey are most amenable for studies of multiple systems that have separate disks, but common-envelopes.

A detailed study of an unusual triple system, WL20, that was part of this survey has shown that disk-disk interaction has resulted in enhanced accretion onto one component of this system, WL20S. This tidally-induced disk disturbance explains the Class I SED of this object, although it is coeval, at an age of several million years, with its Class II SED companions (Ressler & Barsony 2001; Barsony et al. 2002).

A comprehensive study of disk evolution in these multiple systems requires both spatially resolved, multi-wavelength, near-infrared photometry–a challenge at sub-arcsecond separations and at the faint J magnitudes of many of these systems, and spatially resolved near-infrared spectroscopy. Such data have been obtained for a dozen binary systems and

their analysis is the subject of a future work (Barsony et al. 2005).

5. Summary

We have carried out a high-spatial resolution, ground-based, mid-infrared imaging survey of 172 objects toward the ρ Ophiuchi star-forming cloud core. The target list included 102 objects chosen for their combined properties of infrared brightness (K$\leq$13.0) and red color (H$-$K$\geq$1.67) from the NIR survey of Barsony et al. (1997), augmented by known cloud members inferred from observations at other wavelengths.

Eighty-five of the target objects were detected. The general agreement between the mid-infrared fluxes determined in this study with the *ISOCAM*-determined fluxes for objects common to both surveys is quite good, as is the agreement for objects in common to both studies for which only ground-based flux upper limits could be determined. A significant fraction of sources (18 objects) were found to be mid-infrared variables, and a further 19 objects are either extended and/or variable.

A plot of the frequency near- to mid-infrared spectral slopes, a, for the objects with newly determined mid-infrared fluxes, shows 19 Class I, 23 Flat Spectrum, 37 Class II, and 21 Class III objects. It is argued that Flat Spectrum objects represent a distinct evolutionary phase in which the remnant infall envelopes from the Class I phase are dispersed, and, that YSOs spend a significant fraction of time, of order 4×10^5 yr, in this state.

A plot of the spectroscopically determined near-infrared veiling, r_K vs. near- to mid-infrared spectral slope, a, for the detected objects in our survey for which published r_K values are available, is presented. We find a general trend of an increasing r_K *threshold* with increasing a, such that Class I objects *generally* exhibit $r_K \geq 1$, Flat Spectrum objects *generally* have $r_K \geq 0.58$, and Class III objects *generally* have $r_K = 0$. Class II objects, however, have the widest range of r_K values, from $0 \leq r_K \leq 4.5$. The most striking result, however, is the highly variable value of veiling that a single source can exhibit in any of the Class II/Flat Spectrum/Class I phases, signalling the highly time-variable accretion activity in disks.

Finally, to study disk dispersal mechanisms, we present plots of ΔN (mid-IR excess above photospheric emission) vs. Δ K (NIR excess above photospheric emission), for two photospheric models: blackbody and Kurucz model atmospheres. Determinations of the mid-IR and NIR excesses were made for the subset of our mid-IR survey sample for which spectroscopically determined effective temperatures and reliable, previously published, A_V values are available. In all cases, we find no sources occupying the region of the plot that

corresponds to optically thick inner disks with optically thin outer disks. By contrast, the entire region of optically thin inner disks, spanning the range from optically thin to optically thick outer disks, is populated, as is the region with both optically thick inner and outer disks. The results are consistent with disk dispersal proceeding from the inside-out, but further observational investigations to confirm this hypothesis are suggested.

This paper is dedicated to the memory of a dear friend, colleague, and mid-infrared astronomer extraordinaire, Dr. Lynne K. Deutsch, who passed away after a long illness on the night of 2 April 2004.

Financial support through NSF grants AST 00-96087 (CAREER), AST 97-53229 (POWRE), AST 02-06146, the NASA/ASEE Summer Faculty Fellowship program at the Jet Propulsion Laboratory, and NASA's Faculty Fellowship Program at Ames Research Center, have made the completion of this work possible. We wish to thank the staff at the Keck and Palomar observatories for their enthusiasm, patience, and assistance in making it possible to use MIRLIN at these telescopes, and Bob Goodrich for his support with the LWS instrument at Keck I. Development of MIRLIN was supported by the JPL's Director's Discretionary Fund, and its continued operation was funded by an SR+T Award from NASA's Office of Space Science.

Dr. Suzanne Casement, former post-doctoral researcher at U.C. Riverside, Ana Matkovic, former summer undergraduate researcher at Harvey Mudd College, and former HMC undergraduate, Christian Baude, also contributed during the early data reduction phases of this work. Patricia Monger's contributions in systems administration and in providing the plotting program, SM, have been invaluable, and are gratefully acknowledged. We thank the referee, Prof. Bruce Wilking, for his meticulous readings of the manuscript, and for his numerous helpful suggestions for its improvement.

Table 1. Observing Logs & Data Reduction Parameters

U.T. Date of Observation	Telescope	Observed Standards	Standard Star N (Magnitudes)	Standard Star Aperture Radius (arcsec)	Target Object Aperture Radius (arcsec)	Aperture Correction	Airmass Correction (Magnitudes/Airmass)	Zero Point
24 APR 96	P200″			2.1	1.2	1.13±0.046	0.09	13.65
		α Boo	−3.19					
		α Sco	−4.54					
26 JUN 97	P200″			2.1	1.2	1.298±0.104	0.29	13.71
		σ Sco	+2.40					
		α Lyrae	+0.00					
		α Sco	−4.54					
		μ Cep	−3.84					
27 JUN 97	P200″			2.1	1.2	1.268±0.0388	0.25±0.05	13.74
		σ Sco	+2.40					
		α Lyrae	+0.00					
7 JUN 98	Keck II			2.1	0.69	1.134±0.0227	0.00±0.06	15.35±0.04
		α Cr B	+2.19					
		γ Aql	−0.78					
30 JUN 98	P200″			2.1	1.2	1.136±0.029	0.30±0.05	13.94
		ϕ Oph	+2.20					
		WL12	+3.78					
1 JUL 98	P200″			2.1	1.2	1.105±0.018	0.26±0.03	13.87
		μ Cep	−3.84					
		γ Aql	−0.78					
		ϕ Oph	+2.20					
28 JUN 99	LWS/Keck I			2.0	0.72	1.142±0.015	−0.03	13.61
		α Boo	−3.19					
		σ Sco	+2.40					
29 JUN 99	LWS/Keck I			2.0	0.72	1.138±0.058	0.00	13.71±0.02
		μ U Ma	−1.03					
		σ Sco	+2.40					

Table 1—Continued

U.T. Date of Observation	Telescope	Observed Standards	Standard Star N (Magnitudes)	Standard Star Aperture Radius (arcsec)	Target Object Aperture Radius (arcsec)	Aperture Correction	Airmass Correction (Magnitudes/Airmass)	Zero Point

Table 2. Mid-Infrared Fluxes for ρ Oph Sources

BKLT[1]	Aliases	α(2000)	δ(2000)	10.8 μm Flux (Jy)[2,3]	12.5 μm Flux (Jy)[2,3]	Date Obs.	Tel./Inst.
	SR2	16 25 19.45	-24 26 51.5	$\leq$0.033		1JUL98	P200/MIRLIN
162522−243452		16 25 22.75	-24 34 52.7	$\leq$0.014		7JUN98	KeckII/MIRLIN
162536−241544	IRS2	16 25 36.76	-24 15 44.8	0.298		1JUL98	P200/MIRLIN
162542−242712	IRS7	16 25 42.5	-24 27 12.9	$\leq$0.064		1JUL98	P200/MIRLIN
162547−241833	IRS8	16 25 47.7	-24 18 33.6	$\leq$0.033		1JUL98	P200/MIRLIN
162549−243139	IRS9	16 25 49.14	-24 31 39.6	$\leq$0.020		1JUL98	P200/MIRLIN
162550−243913	IRS10	16 25 50.66	-24 39 13.9	$\leq$0.050		1JUL98	P200/MIRLIN
162556−242050	SR4	16 25 56.17	-24 20 50.5	0.81		26JUN97	P200/MIRLIN
162557−243032	IRS13=GSS20	16 25 57.62	-24 30 32.5	$\leq$0.068		1JUL98	P200/MIRLIN
162603−242337	Elias14=DoAr21	16 26 03.01	-24 23 37.9	0.206		30JUN98	P200/MIRLIN
162607−242725		16 26 07.15	-24 27 25.6		0.143	28JUN99	KeckI/LWS
162608−241855	CRBR4	16 26 08.75	-24 18 55.2	$\leq$0.069		30JUN98	P200/MIRLIN
162608−241855	CRBR4	16 26 08.75	-24 18 55.2	$\leq$0.047		7JUN98	KeckII/MIRLIN
162609−243411	SR3	16 26 09.35	-24 34 11.1	0.148		7JUN98	KeckII/MIRLIN
162610−242056	GSS26	16 26 10.28	-24 20 56.6	1.01		27JUN97	P200/MIRLIN
162615−241924	CRBR9	16 26 15.77	-24 19 24.6		$\leq$0.023	29JUN99	KeckI/LWS
162616−242225	Elias18=GSS29	16 26 16.81	-24 22 25.3	0.397		1JUL98	P200/MIRLIN
162616−242225	Elias18	16 26 16.81	-24 22 25.3	0.372		30JUN98	P200/MIRLIN
162617−242023	Elias19	16 26 17.02	-24 20 23.9	0.404		1JUL98	P200/MIRLIN
162617−242347	CRBR12	16 26 17.21	-24 23 47.7	0.315		27JUN97	P200/MIRLIN
162618−242818[4]		16 26 18.09	-24 28 18.1		1.03	28JUN99	KeckI/LWS
162618−241712		16 26 18.60	-24 17 12.7		$\leq$0.003	28JUN99	KeckI/LWS
162618−242416	CRBR15	16 26 18.95	-24 24 16.6		0.074	28JUN99	KeckI/LWS
162618−242310	CRBR17	16 26 18.98	-24 23 10.1	$\leq$0.005		7JUN98	KeckII/MIRLIN
162619−242820	Elias20=VSSG1	16 26 19.03	-24 28 21	0.732		27JUN97	P200/MIRLIN
162620−242840		16 26 20.98	-24 28 40.8	$\leq$0.089		1JUL98	P200/MIRLIN
162621−242306	GSS30 IRS1	16 26 21.42	-24 23 06.4	8.52		7JUN98	KeckII/MIRLIN
162621−242306	GSS30 IRS1	16 26 21.42	-24 23 06.4	8.17		30JUN98	P200/MIRLIN
	GSS30 IRS3	16 26 21.72	-24 22 50.2	$\leq$0.12		30JUN98	P200/MIRLIN
162622−242449	CRBR23	16 26 22.16	-24 24 49.9		$\leq$0.019	28JUN99	KeckI/LWS
162622−242409	GY11	16 26 22.28	-24 24 09.3	$\leq$0.076		1JUL98	P200/MIRLIN
162622−242409	GY11	16 26 22.28	-24 24 09.3	$\leq$0.020		30JUN98	P200/MIRLIN
162622−242721	GY14	16 26 22.96	-24 27 21.7		$\leq$0.059	28JUN99	KeckI/LWS
162623−242101	DoAr24E=Elias22	16 26 23.34	-24 21 01.8			1JUL98	P200/MIRLIN
	DoAr24E(primary)			0.625		1JUL98	P200/MIRLIN
	DoAr24E(secondary)[5]			2.01		1JUL98	P200/MIRLIN
162623−242441	GY21(secondary)	16 26 23.54	-24 24 41.5	0.398		30JUN98	P200/MIRLIN
162623−242441	GY21(secondary)	16 26 23.54	-24 24 41.5	0.39		1JUL98	P200/MIRLIN
162623−242603	DoAr25=GY17	16 26 23.84	-24 43 11.8	0.26		1JUL98	P200/MIRLIN
162624−242449	Elias23=GY23	16 26 24.05	-24 24 49.7			1JUL98	P200/MIRLIN
162624−242449	Elias23(primary)			2.15		1JUL98	P200/MIRLIN
162624−241616	Elias24	16 26 24.07	-24 16 16.1	2.57		26JUN97	P200/MIRLIN
162625−242446	GY29	16 26 25.28	-24 24 46.7	$\leq$ 0.043		7JUN98	KeckII/MIRLIN
162625−242325	GY31	16 26 25.24	-24 23 25.7	$\leq$0.021		7JUN98	KeckII/MIRLIN
162628−242153	GY38	16 26 28.43	-24 21 53.4		$\leq$0.050	29JUN99	KeckI/LWS

Table 2—Continued

BKLT[1]	Aliases	α(2000)	δ(2000)	10.8 μm Flux (Jy)[2,3]	12.5 μm Flux (Jy)[2,3]	Date Obs.	Tel./Inst.
162628−242153	GY38	16 26 28.43	-24 21 53.4	≤0.042		7JUN98	KeckII/MIRLIN
162629−241908	SKS1-19	16 26 29.6	-24 19 08.0	≤0.079		27JUN97	P200/MIRLIN
162630−243841	GY45[4]	16 26 30.16	-24 38 41.1		≤0.070	29JUN99	KeckI/LWS
162630−243841	GY45[4]	16 26 30.16	-24 38 41.1		≤0.041	28JUN99	KeckI/LWS
162630−242258	GY51=VSSG27	16 26 30.49	-24 22 59			7JUN98	KeckII/MIRLIN
	GY51(primary)			0.224		7JUN98	KeckII/MIRLIN
	GY51(secondary)			≤0.018		7JUN98	KeckII/MIRLIN
162631−243105	IRS14	16 26 31.17	-24 31 05.6	≤0.068		27JUN97	P200/MIRLIN
162631−243141	IRS15=GY58	16 26 31.77	-24 31 41.8	≤0.060		1JUL98	P200/MIRLIN
162633−243625	GY65[4]	16 26 33.0	-24 36 25.9		≤0.044	29JUN99	KeckI/LWS
162634−242330	Elias25=S1=GY70	16 26 34.17	-24 23 30.5	0.065		7JUN98	KeckII/MIRLIN
162637−242302	GY81	16 26 37.8	-24 23 02.6		0.103	28JUN99	KeckI/LWS
162640−242715	GY91=CRBR42	16 26 40.53	-24 27 15.9	0.157		27JUN97	P200/MIRLIN
162641−241801		16 26 41.91	-24 18 02.0		≤0.043	28JUN99	KeckI/LWS
162642−243325	WL8	16 26 42.15	-24 33 25.5	0.0733		7JUN98	KeckII/MIRLIN
162642−243103	WL7	16 26 42.28	-24 31 03.3	0.0514		7JUN98	KeckII/MIRLIN
162642−242627	GY101	16 26 42.50	-24 26 27.4	≤0.021		27JUN97	P200/MIRLIN
162642−242633	GY103	16 26 42.58	-24 26 33.3	≤0.021		27JUN97	P200/MIRLIN
162642−242633	GY103	16 26 42.58	-24 26 33.3		≤0.005	28JUN99	KeckI/LWS
162642−242031	Elias26	16 26 42.81	-24 20 31.9	0.41		1JUL98	P200/MIRLIN
	Elias26(primary)			0.41		1JUL98	P200/MIRLIN
	Elias26(secondary)			≤0.14		1JUL98	P200/MIRLIN
162643−241635	IRS19=VSSG11	16 26 43.67	-24 16 35.7	≤0.038		1JUL98	P200/MIRLIN
162644−243447	WL12	16 26 44.3	-24 34 47.5	1.14		1JUL98	P200/MIRLIN
162644−243447	WL12	16 26 44.3	-24 34 47.5	1.05		7JUN98	KeckII/MIRLIN
162644−243447	WL12	16 26 44.3	-24 34 47.5		0.888/0.967	29JUN99	KeckI/LWS
162645−242309	Elias27	16 26 45.01	-24 23 09.6	0.32		1JUL98	P200/MIRLIN
162646−241203	VSS27	16 26 46.31	-24 12 03.5	0.285		1JUL98	P200/MIRLIN
162646−241203	VSS27	16 26 46.31	-24 12 03.5		0.296	28JUN99	KeckI/LWS
	WL2	16 26 48.56	-24 28 40.4	0.184		24APR96	P200/MIRLIN
	WL2	16 26 48.56	-24 28 40.4	0.155		7JUN98	KeckII/MIRLIN
162648−242836	WL2N (secondary)			≤0.029		24APR96	P200/MIRLIN
162648−242836	WL2N			0.0163		7JUN98	KeckII/MIRLIN
162648−242840	WL2S (primary)			0.186		24APR96	P200/MIRLIN
162648−242840	WL2S			0.139		7JUN98	KeckII/MIRLIN
162648−242626	GY130	16 26 48.8	-24 26 26.8	≤0.023		7JUN98	KeckII/MIRLIN
162649−243823	WL18	16 26 49.19	-24 38 23.7			24APR96	P200/MIRLIN
162649−243823	WL18	16 26 49.19	-24 38 23.7			7JUN98	KeckII/MIRLIN
	WL18N(secondary)			≤ 0.041		24APR96	P200/MIRLIN
	WL18N			≤0.015		7JUN98	KeckII/MIRLIN
	WL18S(primary)			≤ 0.041		24APR96	P200/MIRLIN
	WL18S			0.063		7JUN98	KeckII/MIRLIN
162653−243236	GY146	16 26 53.59	-24 32 36.5	≤0.0285		7JUN98	KeckII/MIRLIN
162653−242229	GY150=VSSG6[4]	16 26 53.85	-24 22 29.7	≤0.065		1JUL98	P200/MIRLIN
162654−242622	GY153=VSSG5	16 26 54.51	-24 26 22.3	≤0.078		27JUN97	P200/MIRLIN

Table 2—Continued

BKLT[1]	Aliases	α(2000)	δ(2000)	10.8 μm Flux (Jy)[2,3]	12.5 μm Flux (Jy)[2,3]	Date Obs.	Tel./Inst.
162654−242703	GY154	16 26 54.84	-24 27 04.0		≤0.065	28JUN99	KeckI/LWS
162654−242231	GY156	16 26 54.97	-24 22 31.4	≤0.076		1JUL98	P200/MIRLIN
162655−242030	GSS41=GY157	16 26 55.27	-24 20 30.3	≤0.039		27JUN97	P200/MIRLIN
162656−242838	GY163	16 26 56.99	-24 28 38.7		≤0.030	28JUN99	KeckI/LWS
162657−243538	WL21	16 26 57.44	-24 35 38.5	≤ 0.026		24APR96	P200/MIRLIN
162657−243538	WL21	16 26 57.44	-24 35 38.5	≤0.038		7JUN98	KeckII/MIRLIN
162657−243538	WL21	16 26 57.44	-24 35 38.5		≤0.020	29JUN99	KeckI/LWS
162658−244529	SR24N(secondary)	16 26 58.46	-24 45 29.9	1.40		26JUN97	P200/MIRLIN
162658−244529	SR24N	16 26 58.46	-24 45 29.9	1.40		7JUN98	KeckII/MIRLIN
162658−244534	SR24S(primary)	16 26 58.20	-24 45 34.7	2.01		26JUN97	P200/MIRLIN
162658−244534	SR24S	16 26 58.52	-24 45 34.7	1.655		7JUN98	KeckII/MIRLIN
162659−243556	WL14	16 26 59.10	-24 35 56.5	≤ 0.037		24APR96	P200/MIRLIN
162659−243556	WL14	16 26 59.10	-24 35 56.5		≤0.022	29JUN99	KeckI/LWS
162659−243556	WL14	16 26 59.1	-24 35 56.5	≤0.0146		7JUN98	KeckII/MIRLIN
162659−243458	WL22	16 26 59.21	-24 34 58.2	0.476		24APR96	P200/MIRLIN
162659−243458	WL22	16 26 59.21	-24 34 58.2	0.443		30JUN98	P200/MIRLIN
162659−243458	WL22	16 26 59.21	-24 34 58.2		0.373/0.560	29JUN99	KeckI/LWS
162701−242138	GY181	16 27 01.56	-24 21 38.3	≤0.10		1JUL98	P200/MIRLIN
162702−243726	WL16[6]	16 27 02.35	-24 37 26.5	6.83		24APR96	P200/MIRLIN
162702−243726	WL16[6]	16 27 02.35	-24 37 26.5	5.94		30JUN98	P200/MIRLIN
162703−242615	GY188	16 27 03.03	-24 26 15.8	≤0.069		27JUN97	P200/MIRLIN
162704−242830	WL1	16 27 04.13	-24 28 30.7	0.130		7JUN98	KeckII/MIRLIN
	WL1N(secondary)			0.050		7JUN98	KeckII/MIRLIN
	WL1S(primary)			0.080		7JUN98	KeckII/MIRLIN
162704−242716	GY195	16 27 04.57	-24 27 16.5	0.059		7JUN98	KeckII/MIRLIN
	LFAM26/GY197	16 27 05.25	-24 36 29.4	≤0.042		30JUN98	P200/MIRLIN
	LFAM26/GY197	16 27 05.25	-24 36 29.4	≤0.102		1JUL98	P200/MIRLIN
162705−242036	GY200	16 27 05.28	-24 20 36.2		≤0.052	29JUN99	KeckI/LWS
162705−242619	IRS30=GY203	16 27 05.97	-24 26 19.3	≤0.038		7JUN98	KeckII/MIRLIN
162705−242619	IRS30	16 27 05.97	-24 26 19.3	≤0.117		1JUL98	P200/MIRLIN
162705−242619	IRS30	16 27 05.97	-24 26 19.3		≤0.093	29JUN99	KeckI/LWS
162706−242837	GY202	16 27 06	-24 28 37.3	≤0.04		1JUL98	P200/MIRLIN
162706−243814	WL17	16 27 06.79	-24 38 14.6		0.825	29JUN99	KeckI/LWS
162709−243408	WL10	16 27 09.13	-24 34 08.1	0.163		7JUN98	KeckII/MIRLIN
162709−244022	GY213	16 27 09.35	-24 40 22.5		0.154	28JUN99	KeckI/LWS
162709−243718	WL15	16 27 09.43	-24 37 18.5	24.2		7JUN98	KeckII/MIRLIN
162709−243718	WL15	16 27 09.43	-24 37 18.5	23.7		26JUN97	P200/MIRLIN
162709−242955	GY215	16 27 09.74	-24 29 55.8	≤0.015		7JUN98	KeckII/MIRLIN
162709−242955	GY215	16 27 09.74	-24 29 55.8		≤0.087	29JUN99	KeckI/LWS
162710−241914	SR21N(primary)	16 27 10.17	-24 19 14.8	1.73		26JUN97	P200/MIRLIN
162710−241921	SR21S(secondary)			≤0.211		26JUN97	P200/MIRLIN
162710−241921	SR21S	16 27 10.14	-24 19 21.2		≤0.024	28JUN99	KeckI/LWS
162710−243322	WL9	16 27 10.39	-24 33 22.6	≤0.0435		7JUN98	KeckII/MIRLIN
162710−243322	WL9	16 27 10.39	-24 33 22.6		≤0.023	29JUN99	KeckI/LWS
162711−244046	GY224	16 27 11.17	-24 40 46.7	0.255		7JUN98	KeckII/MIRLIN

Table 2—Continued

BKLT[1]	Aliases	α(2000)	δ(2000)	10.8 μm Flux (Jy)[2,3]	12.5 μm Flux (Jy)[2,3]	Date Obs.	Tel./Inst.
162711−242343	IRS32=GY228	16 27 11.68	-24 23 43.5	≤0.049		1JUL98	P200/MIRLIN
162711−243832	WL19	16 27 11.74	-24 38 32.1	0.13		24APR96	P200/MIRLIN
162711−243832	WL19	16 27 11.74	-24 38 32.1		0.223	29JUN99	KeckI/LWS
162712−243449	WL11	16 27 12.16	-24 34 49.3	0.0299		7JUN98	KeckII/MIRLIN
162713−244133	GY232[4]	16 27 13.25	-24 41 33.3	0.031		7JUN98	KeckII/MIRLIN
162714−242646	IRS33=GY236	16 27 14.53	-24 26 46.9	0.062		7JUN98	KeckII/MIRLIN
162715−242640	IRS34	16 27 15.48	-24 26 40.6	0.172		7JUN98	KeckII/MIRLIN
	IRS34N(primary)			0.092		7JUN98	KeckII/MIRLIN
	IRS34S(secondary)			0.080		7JUN98	KeckII/MIRLIN
162715−243054	CRBR70=IRS35	16 27 15.54	-24 30 54.1	≤ 0.033		27JUN97	P200/MIRLIN
162715−243843	WL20[7]	16 27 15.83	-24 38 43.6	0.41		24APR96	P200/MIRLIN
162715−243843	WL20[7]	16 27 15.83	-24 38 43.6	0.55		1JUL98	P200/MIRLIN
	WL20S	16 27 15.72	-24 38 45.6	0.281		24APR96	P200/MIRLIN
	WL20S	16 27 15.72	-24 38 45.6	0.350		1JUL98	P200/MIRLIN
	WL20E	16 27 15.89	-24 38 43.4	0.079		24APR96	P200/MIRLIN
	WL20E	16 27 15.89	-24 38 43.4	0.117		1JUL98	P200/MIRLIN
	WL20W	16 27 15.69	-24 38 43.4	0.0515		24APR96	P200/MIRLIN
	WL20W	16 27 15.69	-24 38 43.4	0.082		1JUL98	P200/MIRLIN
162715−242514	IRS36=GY241	16 27 15.88	-24 25 14.8	≤0.017		7JUN98	KeckII/MIRLIN
162717−242856	GY244[8]	16 27 17.60	-24 28 56.6	0.194		24APR96	P200/MIRLIN
162717−242856	GY244[8]	16 27 17.60	-24 28 56.6		0.37	28JUN99	KeckI/LWS
162718−242853	WL5[8]	16 27 18.19	-24 28 53.1	≤0.033		24APR96	P200/MIRLIN
162718−242853	WL5[8]	16 27 18.19	-24 28 53.1		0.05	28JUN99	KeckI/LWS
162718−243915	GY245	16 27 18.38	-24 39 15	0.068		7JUN98	KeckII/MIRLIN
162718−242427	GY248	16 27 18.39	-24 24 27.6		≤0.029	28JUN99	KeckI/LWS
162718−242906	WL4[8]	16 27 18.50	-24 29 6.1	0.292		24APR96	P200/MIRLIN
162718−242906	WL4[8]	16 27 18.50	-24 29 06.1		0.40	28JUN99	KeckI/LWS
162719−242844	WL3[8]	16 27 19.23	-24 28 44.3	0.162		27JUN97	P200/MIRLIN
162719−242844	WL3[8]	16 27 19.23	-24 28 44.3		0.132	28JUN99	KeckI/LWS
162719−244139	SR12	16 27 19.55	-24 41 40	≤ 0.30		26JUN97	P200/MIRLIN
162721−244142	IRS42	16 27 21.45	-24 41 42.8	2.03		27JUN97	P200/MIRLIN
162721−242151	GY255	16 27 21.65	-24 21 51.6		≤0.062	29JUN99	KeckI/LWS
162721−244335	GY253	16 27 21.81	-24 43 35.8	≤0.011		7JUN98	KeckII/MIRLIN
162721−244335	GY253	16 27 21.81	-24 43 35.8		≤0.066	29JUN99	KeckI/LWS
162721−242953	WL6	16 27 21.83	-24 29 53.2	1.08		24APR96	P200/MIRLIN
162721−242953	WL6	16 27 21.83	-24 29 53.2	1.012		7JUN98	KeckII/MIRLIN
162722−242939	GY256	16 27 22.0	-24 29 39.9	1.03		7JUN98	KeckII/MIRLIN
162722−241759	VSSG22	16 27 22.82	-24 17 59.3		≤0.053	29JUN99	KeckI/LWS
162724−242929	GY257	16 27 24.23	-24 29 29.6	≤0.023		7JUN98	KeckII/MIRLIN
162724−244147	GY258	16 27 24.38	-24 41 47.4	≤0.051		1JUL98	P200/MIRLIN
162724−244103	CRBR85	16 27 24.58	-24 41 3.6	0.216		27JUN97	P200/MIRLIN
162724−242935	GY259	16 27 24.66	-24 29 35.4	≤0.015		7JUN98	KeckII/MIRLIN
162726−244246	GY260	16 27 26.27	-24 42 46.4		0.059	29JUN99	KeckI/LWS
162726−243923	GY262	16 27 26.45	-24 39 23.9	0.177		7JUN98	KeckII/MIRLIN
162726−244045	GY263	16 27 26.6	-24 40 45.9	0.03		7JUN98	KeckII/MIRLIN

Table 2—Continued

BKLT[1]	Aliases	α(2000)	δ(2000)	10.8 μm Flux (Jy)[2,3]	12.5 μm Flux (Jy)[2,3]	Date Obs.	Tel./Inst.
162726−244051	IRS43=GY265	16 27 26.9	-24 40 51.5	2.29		27JUN97	P200/MIRLIN
162726−244051	IRS43=GY265	16 27 26.9	-24 40 51.5	1.54		7JUN98	KeckII/MIRLIN
162727−243217	GY266	16 27 27.12	-24 32 17.8	≤0.044		1JUL98	P200/MIRLIN
162727−243116	WL13	16 27 27.43	-24 31 16.9	0.085		7JUN98	KeckII/MIRLIN
162728−243934	IRS44=YLW16A	16 27 28.0	-24 39 34.3	2.65		27JUN97	P200/MIRLIN
162728−243143	GY272	16 27 28.2	-24 31 43.7	≤0.030		1JUL98	P200/MIRLIN
162728−242721	Elias32=IRS45	16 27 28.44	-24 27 21.9	0.41		26JUN97	P200/MIRLIN
162728−241709		16 27 28.64	-24 17 09.4		≤0.005	28JUN99	KeckI/LWS
162729−243408	GY275	16 27 29.35	-24 34 08.0		≤0.029	28JUN99	KeckI/LWS
162729−243917	IRS46	16 27 29.41	-24 39 17	0.540		7JUN98	KeckII/MIRLIN
162730−242744	Elias33=GY279	16 27 30.18	-24 27 44.3	0.954		27JUN97	P200/MIRLIN
162730−243335	GY278	16 27 30.21	-24 33 36	≤0.043		27JUN97	P200/MIRLIN
162732−242943	GY287	16 27 32.16	-24 29 43.6		≤0.037	28JUN99	KeckI/LWS
162732−244500	GY288	16 27 32.74	-24 45 0.5	≤0.007		7JUN98	KeckII/MIRLIN
162732−243323	GY289	16 27 32.75	-24 33 23.5		≤0.039	28JUN99	KeckI/LWS
162732−243242	GY290	16 27 32.79	-24 32 42.5		≤0.030	28JUN99	KeckI/LWS
162732−243235	GY291	16 27 32.92	-24 32 35.0		0.087	28JUN99	KeckI/LWS
162733−241115	GY292=CRBR90	16 27 33.11	-24 41 15.7		0.551/0.699	29JUN99	KeckI/LWS
162737−242846	GY303	16 27 37.12	-24 28 46.2	≤0.08		27JUN97	P200/MIRLIN
162737−243035	IRS48	16 27 37.23	-24 30 35.2	3.91		30JUN98	P200/MIRLIN
162737−243035	IRS48	16 27 37.23	-24 30 35.2		2.07/2.61	29JUN99	KeckI/LWS
162737−244238	GY301	16 27 37.28	-24 42 38.7	≤0.047		27JUN97	P200/MIRLIN
162738−242528	GY309	16 27 38.05	-24 25 28.8	≤0.001		7JUN98	KeckII/MIRLIN
162738−242528	GY309	16 27 38.05	-24 25 28.8		≤0.035	29JUN99	KeckI/LWS
162738−243043	IRS50=GY306	16 27 38.17	-24 30 43.1	≤0.097		1JUL98	P200/MIRLIN
162738−243658	IRS49	16 27 38.4	-24 36 58.3	0.425		26JUN97	P200/MIRLIN
162739−243914	GY314	16 27 39.46	-24 39 14.7		0.664	28JUN99	KeckI/LWS
162739−244316	IRS51	16 27 39.84	-24 43 16.1	1.10		26JUN97	P200/MIRLIN
162740−242205	SR9	16 27 40.3	-24 22 05.5	0.43		26JUN97	P200/MIRLIN
162741−244337	GY323	16 27 41.76	-24 43 37.3	0.045		7JUN98	KeckII/MIRLIN
162743−244309	IRS53=GY334	16 27 43.81	-24 43 09.4	≤0.064		7JUN98	KeckII/MIRLIN
162743−244309	IRS53=GY334	16 27 43.81	-24 43 09.4		≤0.016	29JUN99	KeckI/LWS
162745−244454	GY344	16 27 45.84	-24 44 54.6		0.117	28JUN99	KeckI/LWS
162746−243759	GY346	16 27 46.03	-24 37 59.7		≤0.021	29JUN99	KeckI/LWS
162746−242323	Elias35=GY351[4]	16 27 46.70	-24 23 23.8	≤0.052		1JUL98	P200/MIRLIN
162747−244535	GY352	16 27 47.16	-24 45 35.5		0.052/0.073	29JUN99	KeckI/LWS
162749−242522	GY 371	16 27 49.78	-24 25 22.9	≤0.25		1JUL98	P200/MIRLIN
162750−244822	WLY54	16 27 50.87	-24 48 22.4	≤ 0.63		26JUN97	P200/MIRLIN
162751−243145	IRS54	16 27 51.89	-24 31 45.8	2.51		26JUN97	P200/MIRLIN
162752−244049	IRS55=GY380	16 27 52.12	-24 40 49.8	≤0.094		1JUL98	P200/MIRLIN
162752−244049	IRS55	16 27 52.12	-24 40 49.8	≤ 0.34		26JUN97	P200/MIRLIN
162755−242619	SR10=GY400	16 27 55.49	-24 26 19.0	0.181		1JUL98	P200/MIRLIN
162803−243441	GY450	16 28 03.66	-24 34 41.6	≤0.060		1JUL98	P200/MIRLIN
162804−243451	GY461	16 28 04.65	-24 34 51.6	≤0.057		1JUL98	P200/MIRLIN
162804−243459	GY463	16 28 04.74	-24 34 59.2	≤0.008		7JUN98	KeckII/MIRLIN

Table 2—Continued

BKLT[1]	Aliases	α(2000)	δ(2000)	10.8 μm Flux (Jy)[2,3]	12.5 μm Flux (Jy)[2,3]	Date Obs.	Tel./Inst.
162836−243552		16 28 36.61	-24 35 52.8		≤0.40	29JUN99	KeckI/LWS
162841−241618		16 28 41.73	-24 16 18.5	≤0.007		7JUN98	KeckII/MIRLIN
162841−241618		16 28 41.73	-24 16 18.5		≤0.023	29JUN99	KeckI/LWS
162904−244057		16 29 04.01	-24 40 57.3		≤0.060	28JUN99	KeckI/LWS
162923−241359	WLY64=IRAS64a	16 29 23.39	-24 13 59.2	0.63		26JUN97	P200/MIRLIN
162923−241359	WLY64	16 29 23.39	-24 13 59.2	0.478		1JUL98	P200/MIRLIN

[1]Source designations from Barsony et al. (1997)

[2]Upper limits are 3 σ

[3]Where 2 values of 12.5 μm flux are listed, separated by a forward-slash, the first flux is measured in a circular aperture of radius 0.72″, the second in a circular aperture of radius 2.0″. Such objects are likely extended in the mid-infrared at these angular scales.

[4]Spectroscopically determined background giant (Luhman & Rieke 1999)

[5]The secondary in the DoAr24E system is an Infrared Companion discovered by Chelli et al. (1988).

[6]WL16 and its extended PAH & VSG disk are thoroughly discussed in Ressler & Barsony (2003); the aperture photometry presented here was measured in r= 4″ and r= 3.75″ circular apertures, for the data of 24 April 1996 and 30 June 1998, respectively.

[7]The combined flux of the WL20 triple system is listed here. See Ressler & Barsony (2001) for a thorough discussion of this system. Individual source positions for each component are from Barsony, Greene, & Blake (2002).

[8]Our chop/nod directions and separations were poorly placed with respect to the WL3, WL4, WL5, & GY244 asterism. Hence, we quote an upper limit for WL5 derived from the average values for undetected sources for 24 April 1996, instead of measuring an upper limit directly from the co-added data for this source.

Table 3. Mid-Infrared Variables in Ophiuchus

BKLT	Aliases	MIRLIN Flux (Jy)	ISOCAM 10.8 μm Flux (Jy)	LWS Flux (Jy)	ISOCAM 12.5 μm Flux (Jy)	Previous Ground-Based Flux (Jy)
162536−241544	IRS 2	0.298 ± 0.007	0.207 ± 0.019			0.206 ± 0.029[1]
162556−242050	SR4/IRS 12	0.810 ± 0.020	0.541 ± 0.023			0.994 ± 0.029[1]
						0.75±0.14, 0.82 ±0.15[2]
162603−242337	DoAr 21	0.206 ± 0.005	0.417 ± 0.015			0.43 ± 0.065[3]
162610−242056	GSS 26	1.01 ± 0.025	0.410 ± 0.010			0.98 ± 0.15[3]
162617−242023	DoAr 24/Elias 19	0.404 ± 0.010	0.225 ± 0.003			0.59 ± 0.12[2]
						0.90 ± 0.16[2]
162621−242306	GSS 30/IRS 1	8.52 ± 0.157	12.19 ± 0.151			11.48 ± 1.05[4]
162642−242031(primary)	Elias 26	0.410 ± 0.010	0.287 ± 0.005			
162644−243447	WL 12	1.05 ± 0.020	1.97 ± 0.025			1.74±0.26[3]
162706−243814	WL 17			0.825 ± 0.045	0.665 ± 0.012	0.35 ± 0.09[3]
162649−243823(primary)	WL 18	0.063 ± 0.001	0.093 ± 0.001	0.070 ± 0.004	0.090 ± 0.002	
162658−244534[6]	SR24	3.055 ± 0.0563	1.885 ± 0.101			1.95 ± 0.04[1]
						2.9 ± 0.55[2]
						3.95±0.26[5]
162709−244022	GY 213			0.154 ± 0.009	0.092 ± 0.003	
162710−241914(primary)	SR21	1.73 ± 0.043	2.255 ± 0.018			
162711−244046	GY 224	0.255 ± 0.005	0.313 ± 0.006			0.23 ± 0.046[5]
162711−243832	WL 19	0.130 ± 0.003	0.174 ± 0.007	0.223 ± 0.013	0.151 ± 0.009	
162714−242646	IRS 33	0.062 ± 0.001	0.109 ± 0.006			
162715−242640	IRS 34			0.084 ± 0.005	0.156 ± 0.011	0.23 ± 0.02[1]
162715−243843[7]	WL 20	0.411 ± 0.010	0.491 ± 0.006			0.18±0.03[3]
162717−242856	GY 244	0.194 ± 0.005	0.319 ± 0.007			
162718−243915	GY 245	0.068 ± 0.005	<0.013 ± 0.001[8]			
162718−242906	WL 4			0.400 ± 0.023	0.275 ± 0.010	0.18 ± 0.03[3]
162719−242844	WL 3	0.162 ± 0.004	0.249 ± 0.008	0.132 ± 0.007	0.234 ± 0.006	0.13 ± 0.02[3]

Table 3—Continued

BKLT	Aliases	MIRLIN Flux (Jy)	ISOCAM 10.8 μm Flux (Jy)	LWS Flux (Jy)	ISOCAM 12.5 μm Flux (Jy)	Previous Ground-Based Flux (Jy)
162724−244103	CRBR 85	0.216 ± 0.005	0.277 ± 0.009			
162726−243923	GY262/CRBR 88	0.177 ± 0.003	0.180 ± 0.011			0.044 ± 0.009[5]
162726−244051	IRS 43	2.29 ± 0.056	3.408 ± 0.050			1.98 ± 0.18[1]
162728−-243934	IRS 44	2.65 ± 0.065	8.08 ± 0.091			5.03 ± 0.46[1]
162730−242744	Elias 33/IRS 47	0.954 ± 0.023	1.651 ± 0.012		0.64 ± 0.096[3]	
162733−241115	GY292/CRBR 90	0.699 ± 0.013	0.468 ± 0.008			0.75 ± 0.15[5]
162737−243035	IRS 48	3.910 ± 0.010	6.204 ± 0.074	2.61±0.145	6.343 ± 0.080	5.67±0.53[1]
162738−243658	IRS 49	0.425 ± 0.011	0.319 ± 0.031			0.61±0.056[1]
162737−244238	GY 301	≤0.047 ± 0.005	0.120 ± 0.005			
162739−243914	GY 314			0.664 ± 0.037	0.377 ± 0.006	0.43 ± 0.086[5]
162745−244454	GY 344			0.117 ± 0.007	0.077 ± 0.003	
162747−244535	GY 352			0.073 ± 0.004	0.039 ± 0.005	
162751−243145	IRS 54	2.51 ± 0.062	5.00 ± 0.073			11.73±1.08[1]
162755−242619	SR10/GY 400	0.181 ± 0.005	0.101 ± 0.003			0.20 ± 0.04[5]
162923−241359	IRAS 64a	0.63/0.48 ± 0.005				0.39 ± 0.07[5]

[1]Flux from Table 2 of Wilking, Lada, & Young (1989)

[2]Flux from Table 4 of Rydgren, Strom, & Strom (1976)

[3]Flux from Table 1 of Lada & Wilking (1984)

[4]Flux from Table 2 of Elias (1978)

[5]Flux from Table 1 of Greene et al. (1994)

[6]The SR24 system is a hierarchical triple, with a 6.0″ separation between the primary, SR24S (=BKLT J162658−244534), and the

secondary, SR24N (= BKLT J162658−244529), which itself consists of a 0.20″ separation binary. Although SR24S & SR24N were unresolved by *ISOCAM*, previous ground-based observations did resolve these components. N-band fluxes for SR24S are 0.78 ± 0.029 Jy (WLY89) and 2.28±0.21 Jy (GWAYL94), to be compared with MIRLIN fluxes of 2.01 Jy and 1.66 Jy for SR24S on 26 June 1997 and 7 June 1998, respectively. N-band fluxes for SR24N are 1.17 ± 0.029 Jy (WLY89) and 1.67±0.16 Jy (Greene et al. 1994), to be compared with the MIRLIN flux of 1.40 Jy for both dates of observation. Therefore, we can conclude that it is the single, primary star in this system, SR24S, which is the mid-infrared variable.

[7]WL20 (= BKLT J162715−243843) is a triple system, which was noted as highly variable in unresolved *ISOCAM* 6.7 μm measurements. The previously published N-band flux for the WL20 system from ground-based measurements was 0.180 ± 0.03 Jy (LW84). Our observations resolve the triple system in the mid-infrared, and show that it is the "infrared companion", WL20S, which is the mid-infrared variable (see Table 2).

[8]*ISOCAM* data from Wilking et al. (2001).

Table 4. ρ Oph Source Properties

BKLT	Aliases	K (mag)	H−K (mag)	α^1_{IR}	SED	r^2_K	A^2_V (mag)
162722−242939	GY256	12.75	2.79	+2.35	I	···	···
162751−243145	IRS54	10.87	2.63	+1.77	I	>2	···
162724−244103	CRBR85	13.21	≥ 2.29	+1.59	I	···	···
162715−243843	WL20						
	WL20S	12.57	1.88	+1.38	I	< 0.9 (BGB02)	41.3 (BGB02)
162709−243718	WL15	7.54	4.47	+1.27	I	> 2	$11.1 \leq A_V \leq 17.0$ (B02)
162729−243917	IRS46/YLW16B	11.46	3.19	+1.15	I	> 1	···
162617−242347	CRBR12	12.04	3.54	+1.15	I	2.0 (D04)	···
162728−243934	IRS44/YLW16A	9.65	3.44	+1.10	I	1, 2.2 (D04)	···
162621−242306	GSS30 IRS1/GY6	8.32	2.51	+1.04	I	> 2	···
162640−242715	GY91/CRBR42	12.51	≥2.99	+0.98	I	0.3 (D04)	···
162726−244051	IRS43/GY265	9.46	3.71	+0.90	I	3 (GL02), 1.7(PGS03)	38 (PGS03)
162644−243447	WL12	10.18	2.89	+0.88	I	1−3	···
162721−242953	WL6	10.04	4.35	+0.76	I	> 4.6 (GL02)	···
162706−243814	WL17	10.28	3.29	+0.60	I	3.9 (D04)	···
162630−242258	GY51/VSSG27					2.0, 0.5, 2.3 (GM95)	22 (GM95)
	GY51/VSSG27 SW(primary)	11.14	3.59	+0.46	I		
162610−242056	GSS26	9.38	2.25	+0.34	I	4, 0.75	21.3
162745−244454	GY344	11.84	2.21	+0.30	F.S.	···	···
162726−244246	GY260	12.54	3.17	+0.28	F.S.	···	···
162719−242844	WL3	11.20	3.29	+0.24	F.S.	1.0 (GM95)	···
162714−242646	IRS33/GY236	12.23	3.04	+0.23	F.S.	···	···
162721−244142	IRS42	8.41	2.90	+0.22	F.S.	> 1	···
162717−242856	GY244	10.95	2.95	+0.21	F.S.	0	···

Table 4—Continued

BKLT	Aliases	K (mag)	H−K (mag)	α_{IR}^1	SED	r_K^2	A_V^2 (mag)
162711−244046	GY224	10.79	2.90	+0.21	F.S.	> 0.5	···
162648−242840	WL2S (primary)	10.99	2.06	+0.21	F.S.	1.5 (GM95)	···
162709−244022	GY213	11.32	2.17	+0.19	F.S.	···	···
162718−243915	GY245	11.98	3.45	+0.15	F.S.	···	···
162739−244316	IRS51	8.93	3.49	+0.13	F.S.	1−3	~ 33.7
162711−243832	WL19	11.23	>4.27	+0.12	F.S.	3.7 (D04)	···
162618−242416	CRBR15	11.94	1.95	+0.09	F.S.	0.64(WGM99)	17.7
162623−242441	GY21(secondary)	9.94	1.69	+0.08	F.S.	1, 2.5 (GM95)	13.5, 16 (GL97)
162737−243035	IRS48	7.42	1.23	+0.05	F.S.	···	···
162730−242755	Elias33/GY279/VSSG17	8.95	2.69	+0.05	F.S.	0.75, 1, 2.8 (GM95), 0.5 (D04)	24.5, 28 (GL97)
162715−242640	IRS34	10.66	2.81	−0.03	F.S.	1.8 (GM95)	···
162741−244337	GY323	11.93	2.56	−0.14	F.S.	···	···
162623−242101	DoAr24E/Elias22						
	DoAr24E/Elias22(secondary)	7.81	1.59	−0.14	F.S.	···	16.2
162728−242721	IRS45/VSSG18	9.39	2.09	−0.22	F.S.	0	17.7
162637−242302	GY81/VSSG4	10.92	1.91	−0.26	F.S.	1−2	16.3
162619−242820	Elias20/VSSG1	8.68	2.08	−0.27	F.S.	···	···
162607−242725		10.48	2.02	−0.30	F.S.	···	···
162704−242716	GY195	11.30	2.25	−0.34	II	···	···
162732−243235	GY291	10.89	1.90	−0.37	II	···	···
162726−244045	GY263	11.93	2.76	−0.40	II	···	···
162624−242449	Elias23/GY23 (primary)	7.20	1.48	−0.40	II	0.75, 1.2 (DJW03)	11
162704−242830	WL1						
	WL1S(primary)	10.76	2.08	−0.46	II	0.8 (D04)	···

Table 4—Continued

BKLT	Aliases	K (mag)	H−K (mag)	α_{IR}^{1}	SED	r_K^2	A_V^2 (mag)
162648−242836	WL2N (secondary)	12.48	3.25	−0.46	II	···	···
162726−243923	GY262	9.77	2.30	−0.53	II	1	22.7
162739−243914	GY314	8.35	0.92	−0.55	II	0.5, 1.9(GM95)	7.1, 4.9 (GM95)
162658−244534	SR24S(primary)	7.08	1.17	−0.56	II	1−3, 0.1(GM95)	4.3
162747−244535	GY352	11.04	1.83	−0.59	II	···	···
162718−242906	WL4	9.13	1.93	−0.59	II	0.25, 1.1(GM95)	19
162658−244529	SR24N(secondary)	7.42	1.18	−0.59	II	2, 0.1(GM95)	7
162624−241616	Elias24	6.77	1.46	−0.59	II	1−3, 4.5 (DJW03)	8.2
162712−243449	WL11	11.53	1.76	−0.63	II	···	···
162645−242309	Elias27	8.88	1.62	−0.67	II	0.75, 1.8(GM95)	17, 14 (GM95)
162704−242830	WL1						
	WL1N(secondary)	10.85	2.06	−0.70	II	···	···
162733−241115	GY292/CRBR90	7.92	1.37	−0.75	II	1, 4.0 (DJW03)	10.3
162642−243103	WL7	10.73	2.48	−0.75	II	···	···
162738−243658	IRS49/GY308	8.31	1.24	−0.83	II	0.75, 1.6 (DJW03)	10.3
162715−243843	WL20						
	WL20E	10.13	1.15	−0.83	II	0.2 (BGB02)	16.3 (BGB02)
162642−242031	Elias 26						
	Elias26(primary)	8.30	0.85	−0.85	II	0.06 (PGS03)	11 (PGS03)
162649−243823	WL18						
	WL18S(primary)	10.21	1.35	−0.93	II	>1	9.2
162715−243843	WL20						
	WL20W	10.40	1.18	−0.94	II	0.2 (BGB02)	16.3 (BGB02)
162617−242023	Elias19/GSS28	8.09	0.58	−0.98	II	0.5, 0.1(GM95), 1.2 (DJW03)	2.8

Table 4—Continued

BKLT	Aliases	K (mag)	H−K (mag)	α^1_{IR}	SED	r^2_K	A^2_V (mag)
162616−242225	Elias18/GSS29	8.19	1.04	−0.98	II	0, 0.1(GM95), 0.3 (DJW03)	10.6, 12 (GM95)
162718−242853	WL5	10.28	4.04	−1.01	II	0 (GM95)	51 (GM95)
162536−241544	IRS2	8.36	0.70	−1.02	II	0, 0.1(GM95)	6.7
162556−242050	SR4	7.25	0.72	−1.03	II	1.5, 2, 3.7 (DJW03)	1.8
162755−242619	SR10/GY400	8.74	0.60	−1.11	II	0.5	0
162710−241914	SR21N(primary)	6.30	1.03	−1.11	II	0.78 (PGS03)	9 (PGS03)
162709−243408	WL10	8.85	1.39	−1.12	II	0.75, 0.6 (D04)	12.8
162727−243116	WL13/VSSG25	9.30	1.11	−1.26	II	0.25, 0.5(GM95)	11
162642−243325	WL8	9.44	3.05	−1.28	II	···	···
162623−242101	DoAr24E/Elias22						
	DoAr24E/Elias22(primary)	7.06	0.67	−1.31	II	0, 1.6 (DJW03)	6.4
162740−242205	SR9/Elias34	7.20	0.51	−1.46	II	0.75	0
162646−241203	VSS27	7.51	0.82	−1.54	II	0.75	6.7
162623−242603	DoAr25/GY17	7.57	0.79	−1.56	II	0, 0.1(GM95)	0
162923−241359	WLY64/IRAS64a[3]	6.45	0.91	−1.65	III	···	···
162603−242337	Elias14/DoAr21	6.16	0.59	−2.53	III	0	5.7
162609−243411	SR3	6.42	0.49	−2.58	III	0	8.2
162634−242330	Elias25/S1/GY70	6.32	0.96	−3.16	III	0	10 (BA92)
	GSS30 IRS3 /LFAM1	13.79	···	$\leq +1.55$	···	···	···
	GY197/LFAM26	14.80	$\geq$3.10	$\leq +1.48$	···	1.2 (D04)	···
162631−243141	IRS15/GY58	13.35	1.46	$\leq +0.86$	···	···	···
162803−243441	GY450	13.09	2.32	$\leq +0.71$	···	···	···
162542−242712	IRS7	12.94	0.79	$\leq +0.67$	···	···	···
162737−242846	GY303	12.68	1.84	$\leq +0.66$	···	···	···

Table 4—Continued

BKLT	Aliases	K (mag)	H−K (mag)	α^1_{IR}	SED	r^2_K	A^2_V (mag)
162728−243143	GY272	13.72	1.78	$\leq +0.64$	···	···	···
162622−242409	GY11	14.15	1.22	$\leq +0.64$	···	···	···
162654−242703	GY154	12.91	2.13	$\leq +0.53$	···	···	25 (W01)
162703−242615	GY188	12.52	$\geq$2.98	$\leq +0.47$	···	···	···
162904−244057		12.79	2.28	$\leq +0.42$	···	···	···
162804−243451	GY461	12.65	2.46	$\leq +0.42$	···	···	···
162705−242036	GY200	12.93	1.67	$\leq +0.41$	···	···	···
162706−242837	GY202	12.97	1.70	$\leq +0.39$	···	0.5 (WGM99)	13 (WGM99)
162628−242153	GY38	12.93	2.60	$\leq +0.39$	···	···	···
162608−241855	CRBR4	12.79	$\geq$2.71	$\leq +0.38$	···	···	···
162724−244147	GY258	12.65	2.40	$\leq +0.36$	···	···	···
162653−243236	GY146	13.18	2.32	$\leq +0.30$	···	···	···
162622−242721	GY14	12.44	2.06	$\leq +0.23$	···	···	···
162836−243552		10.37	1.74	$\leq +0.23$	···	···	···
162732−242943	GY287	12.95	2.23	$\leq +0.23$	···	···	···
162732−243242	GY290	13.03	2.85	$\leq +0.18$	···	···	···
162620−242840		11.71	1.61	$\leq +0.16$	···	···	···
162715−243054	CRBR70/IRS35	12.73	$\geq$2.77	$\leq +0.13$	···	···	···
162727−243217	GY266	12.28	2.48	$\leq +0.05$	···	···	···
162730−243335	GY278	12.31	3.26	$\leq +0.05$	···	···	···
162625−242325	GY31	13.09	3.98	$\leq +0.05$	···	···	56 (WGM99)
162729−243408	GY275	12.79	2.01	≤ 0.00	···	···	···
162715−242514	IRS36/GY241	13.18	$\geq$2.32	≤ -0.03	···	···	···
162656−242838	GY163	12.66	2.28	≤ -0.05	···	···	32 (WGM99)

Table 4—Continued

BKLT	Aliases	K (mag)	H−K (mag)	α_{IR}^1	SED	r_K^2	A_V^2 (mag)
162648−242626	GY130	12.79	2.67	≤ -0.07	···	···	···
162749−242522	GY371	10.17	1.04	≤ -0.12	···	···	···
162622−242449	CRBR23	12.97	2.25	≤ -0.14	···	···	···
162629−241908	SKS1−19/LFAM8	11.19	2.05	≤ -0.22	···	0	23.4
162642−242627	GY101	12.58	$\geq$2.92	≤ -0.24	···	···	···
162709−242955	GY215	12.93	2.57	≤ -0.25	···	···	···
162657−243538	WL21	12.67	2.18	≤ -0.27	···	···	···
162724−242929	GY257	12.25	2.71	≤ -0.38	···	···	···
162641−241801		11.63	2.25	≤ -0.38	···	···	···
162746−243759	GY346	12.29	1.48	≤ -0.45	···	···	···
162737−244238	GY301	11.30	3.47	≤ -0.48	···	···	···
162522−243452		12.54	2.50	≤ -0.52	···	···	···
162721−242151	GY255	10.96	1.71	≤ -0.53	···	···	···
162631−243105	IRS14	10.80	1.56	≤ -0.54	···	···	···
162724−242935	GY259	12.41	2.64	≤ -0.55	···	···	···
162750−244822	WLY54	8.23	0.98	≤ -0.62	···	···	···
162710−243322	WL9	11.86	2.11	≤ -0.62	···	···	···
162732−244500	GY288	13.13	2.74	≤ -0.62	···	···	···
162705−242619	IRS30/GY203	11.05	2.52	≤ -0.76	···	···	···
162649−243823	WL18						
	WL18N(secondary)	12.05	1.32	≤ -0.76	···	···	···
162625−242446	GY29	10.86	2.11	≤ -0.79	···	0	22.3
162642−242031	Elias 26						
	Elias26(secondary)	9.56	0.90	≤ -0.80	···	0.22 (PGS03)	14 (PGS03)

Table 4—Continued

BKLT	Aliases	K (mag)	H−K (mag)	α_{IR}^1	SED	r_K^2	A_V^2 (mag)
162654−242231	GY156	10.19	1.78	≤ -0.82	···	0	21.6
162630−242258	GY51/VSSG27					2.0, 0.5, 2.3 (GM95)	22 (GM95)
	GY51/VSSG27 NE(secondary)	11.62	2.87	< -0.85	···		
162718−242427	GY248	11.12	2.13	≤ -0.88	···	···	···
162732−243323	GY289	10.71	1.97	≤ -0.93	···	···	23 (W01)
162659−243556	WL14	11.74	1.64	≤ -0.96	···	0	18
162654−242622	GY153/VSSG5	9.88	1.82	≤ -0.98	···	0.25, 0.1(GM95)	21
162728−241709		12.82	2.04	≤ -0.99	···	···	···
162719−244139	SR12	8.41	0.28	≤ -0.99	···	0	0.7, 1.7 (BA92)
162738−243043	IRS50/GY306	9.59	1.01	≤ -1.01	···	0	11
162701−242138	GY181	9.32	1.74	≤ -1.15	···	···	···
162642−242633	GY103	12.52	$\geq$2.98	≤ -1.15	···	···	···
162711−242343	IRS32/GY228	10.06	1.58	≤ -1.17	···	···	···
162743−244309	IRS53/GY334	11.17	2.76	≤ -1.19	···	···	···
162618−242310	CRBR17	12.32	2.64	≤ -1.30	···	···	···
162722−241759	VSSG22	9.41	1.38	≤ -1.44	···	0	16.3
162841−241618		11.61	2.92	≤ -1.50	···	···	···
162655−242030	GSS41/GY157	9.69	2.13	≤ -1.53	···	···	···
162643−241635	IRS19/VSSG11	9.58	1.27	≤ -1.61	III	0	14.2, 10 (BA92)
162615−241924	CRBR9	9.98	1.46	≤ -1.62	III	0	16.3
162547−241833	IRS8	9.69	1.08	≤ -1.63	III	···	···
162721−244335	GY253	10.78	2.53	≤ -1.69	III	0	29
162804−243459	GY463	10.92	2.48	≤ -1.81	III	···	···
162752−244049	IRS55/GY380	8.09	0.60	≤ -1.90	III	···	···

Table 4—Continued

BKLT	Aliases	K (mag)	H−K (mag)	α_{IR}^1	SED	r_K^2	A_V^2 (mag)
162557−243032	IRS13/GSS20	8.37	0.63	≤ -1.94	III	0, 0.1(GM95)	3.2, 4.3 (BA92)
162710−241921	SR21S(secondary)	9.25	0.75	≤ -1.98	III	0.15 (PGS03)	9.3 (PGS03)
162618−241712		11.45	2.05	≤ -2.01	III	···	···
162738−242528	GY309	12.73	2.91	≤ -2.07	III	···	···
162549−243139	IRS9	9.41	1.21	≤ -2.11	III	···	···
162550−243913	IRS10	8.24	0.45	≤ -2.21	III	···	···
	SR-2	7.82	0.09	≤ -2.67	III	···	0.51 (W94)
162746−242323	Elias35/GY351[4]	7.29	1.12	≤ -2.74	M0 III	···	···

[1]α_{IR} is calculated between 2.2 μm and either 10.8 μm or 12.5 μm, as available from Table 2.

[2]A_V and r_K values are from LR99, unless otherwise indicated.

[3]The nature of WLY64 remains to be clarified, although it is listed as an FU Ori candidate source by LR99.

[4]Spectroscopically determined background giant (Luhman & Rieke 1999).

References. — BKLT = Barsony et al. 1997; B02 = Boogert et al. (2002); BA92 = Bouvier & Appenzeller 1992; BGB02 = Barsony, Greene, & Blake 2002; C88 = Chelli et al. 1988; DJW03 = Doppmann, Jaffe, & White 2003; D04 = Doppmann 2004; GL97 = Greene & Lada 1997; GL02 = Greene & Lada 2002; GM95 = Greene & Meyer 1995; HBGR02 = Haisch et al. 2002; LR99= Luhman & Rieke 1999; PGS03 = Prato, Greene, & Simon 2003; SKS95 = Strom, Kepner, & Strom 1995; W94 = Walter et al. 1994; W01 = Wilking et al. 2001; WGM99 = Wilking, Greene, & Meyer 1999

Table 5. Mid-Infrared Observations of Known Binary/Multiple Systems in Ophiuchus

BKLT	Alias	α(2000)	δ(2000)	System Type[1]	Sep'n. Arcsec	P.A. Deg[2]	Resolved in Mid-IR?
	ROX 1	16 25 19.28	-24 26 52.1	B	0.236	156	N
162536−241544	IRS 2	16 25 36.75	-24 15 42.1	B	0.44+/-0.03	79+/-4	N
162623−242101	DoAr 24E	16 26 23.38	-24 20 59.7	B	2.05	148.6	Y
	Elias23+GY21			B	10.47	322.6	Y
162624−242449	Elias 23	16 26 24.06	-24 24 48.1				
162623−242441	GY 21	16 26 23.60	-24 24 39.4				
162630−242258	VSSG 27	16 26 30.50	-24 22 57.1	B	1.22+/-0.03	68 +/-1	Y
162634−242330	S1	16 26 34.18	-24 23 28.2	B	0.020	110	N
162642−242031	GSS37	16 26 42.87	-24 20 29.8	B(T?)	1.44	67.0	Y
162646−241203	VSS27	16 26 46.44	-24 12 00.0	B	0.59	104.6	N
	WL 2			B	4.17	343	Y
162648−242840	WL 2(A)	16 26 48.50	-24 28 38.7				
162648−242836	WL 2(B)	16 26 48.42	-24 28 34.7				
162649−243823	WL 18	16 26 48.99	-24 38 25.1	B	3.55	293	Y
	SR 24			T	5.093	60	Y
162658−244534	SR 24A	16 26 58.52	-24 45 36.7				
162658−244529	SR 24B	16 26 58.45	-24 45 31.7		0.197	84	N
162704−242830	WL 1	16 27 04.12	-24 28 29.9	B	0.82	321.2	Y
	SR21			B	6.33	175	Y
162710−241914	SR 21A	16 27 10.28	-24 19 12.6				
162710−241921	SR 21B	16 27 10.33	-24 19 18.9				
162715−242640	IRS34	16 27 15.48	-24 26 40.6	B	0.31	236	
162715−243843	WL20			T			
	WL20W	16 27 15.69	-24 38 43.4		3.17 (E-W sep'n.)	270	Y
	WL20S	16 27 15.72	-24 38 45.6		2.26 (S-W sep'n.)	173	Y
	WL20E	16 27 15.89	-24 38 43.4		3.66 (S-E sep'n.)	232	Y
	SR12+IRS42			T			
162719−244139	SR12	16 27 19.55	-24 41 40.0	B	0.30	85	N
162721−244142	IRS42	16 27 21.45	-24 41 42.8		26.8	85.8	Y
	GY263+IRS43			B	6.99	322	Y
162726−244045	GY263	16 27 26.63	-24 40 44.9				
162726−244051	IRS 43	16 27 26.94	-24 40 50.				
	IRS 44+GY262			T(?)			Y
162726−243923	GY262	16 27 26.49	-24 39 23.0		23.21		

Table 5—Continued

BKLT	Alias	α(2000)	δ(2000)	System Type[1]	Sep'n. Arcsec	P.A. Deg[2]	Resolved in Mid-IR?
162728−243934	IRS 44	16 27 28.01	-24 39 33.6	B	0.27	81	N
162727−243116	WL 13	16 27 27.40	-24 31 16.6	B	0.46	356	N
162730−242744	VSSG 17	16 27 30.17	-24 27 43.5	B	0.25	26	N
162740−242205	SR9	16 27 40.28	-24 22 04.3	B	0.59	350	N
162752−244049	ROXs 31	16 27 52.07	-24 40 50.4	B	0.39	71.6	N

[1]B=Binary; SpB=Spectroscopic Binary; T=Triple; Q=Quadruple

[2]PAs are E of N, measured from the primary at K, except for IRS34, where the primary is at N, since no resolved K band data exist

REFERENCES

Armitage, P.J., Clarke, C.J., & Palla, F. 2003, MNRAS, 342, 1139

Barsony, M., Kenyon, S.J., Lada, E.A., & Teuben, P.J. [BKLT] 1997, ApJS, 112, 109

Barsony, M., Greene, T.P., & Blake, G.A. 2002, ApJL, 572, L75

Barsony, M., Koresko, C., & Matthews, K. 2003, ApJ, 591, 1064

Barsony, M., Greene, T.P., & Haisch, K.E. Jr. 2005, in prep.

Bontemps, S., André, Ph., Kaas, A.A., Nordh, L., Olofsson, G., Huldtgren, M., Abergel, A., Blommaert, J., Boulanger, F., Burgdorf, M., Cesarsky, C.J., Cesarsky, D., Copet, E.., Davies, J., Falgarone, E., Lagache, G., Montmerle, T., Pérault, M., Persi, P., Prusti, T., Puget, J.L., & Sibille, F. 2001, A& A, 372, 173

Boogert, A.C.A., Hogerheijde, M.R., Ceccarelli, C., Tielens, A.G.G.M., van Dishoeck, E.F., Blake, G.A., Latter, W.B., & Motte, F. 2002, ApJ, 570, 708

Bouvier, J. & Appenzeller, I. 1992, A & AS, 92, 481

Chelli, A., Cruz-Gonzalez, I., Zinnecker, H., Carrasco, L., & Perrier, C. 1988, A& A, 207, 46

Chiang, E.I. & Goldreich, P. 1997, ApJ, 490, 368

Cohen, J.G., Frogel, J.A., Persson, S.E., & Elias, J.H. 1981, ApJ, 249, 481

Comeron, F., Rieke, G.H., Burrows, A., & Rieke, M. 1993, ApJ, 416, 185

Dent, W.R.F.., Matthews, H.E., & Walther, D.M. 1995, MNRAS, 277, 193

Dolidze, M.V. & Arakelyan, M.A. 1959, A. Zh., 36, 444

Doppmann, G., Jaffe, D., & White, R.J. 2003, AJ, 126, 3043

Doppmann, G. 2004, priv. comm.

Eisner, J.A., Lane, B.F., Akeson, R.L., Hillenbrand, L.A., & Sargent, A.I. 2003 ApJ 588 360

Elias, J. 1978, ApJ, 224, 453

Greene, T.P. & Young, E.T. 1992, ApJ, 395, 516

Greene, T.P., Wilking, B.A., André, Ph., Young, E.T. & Lada, C.J. 1994, ApJ, 434, 614

Greene, T.P. & Meyer, M. R. 1995, ApJ, 450, 233

Greene, T.P. & Lada, C.J. 1997, AJ, 114, 2157

Greene, T.P. & Lada, C.J. 2002, AJ, 124, 2185

Haisch, K.E. Jr., Lada, E.A., Lada, C.J. 2001, ApJL, 553, L153

Haisch, K.E. Jr., Barsony, M., Greene, T.P., & Ressler, M.E. 2002, AJ, 124, 2841

Haisch, K.E. Jr., 2003, priv. comm.

Haisch, K.E. Jr., Greene, T.P., Barsony, M., & Stahler, S.W. 2004, AJ, 127, 1747

Jones, B. & Puetter, R. 1993, Proc. SPIE, 1946, 610

Kamazaki, T., Saito, M., Hirano, N., Umemoto, T., Kawabe, R. 2003, ApJ, 584, 357

Kikuchi, N., Nakamoto, T., Ogoshi, K. 2002, PASJ, 54, 589

Lada, C.J. & Wilking, B.A. 1984, ApJ, 287, 610

Lada, C.J. 1987 in Star Forming Regions, IAU Symposium No. 115, p.1

Leous, J.A., Feigelson, E.D., André, Ph., & Montmerle, T. 1991, ApJ, 379, 683

Looney, L.W., Mundy, L.G., and Welch, W.J. 2000, ApJ, 529, 477

Luhman, K.L. & Rieke, G.H. 1999, ApJ, 525, 440

Millan-Gabet, R. Schloerb, F.P., & Traub, W.A. 2001, ApJ, 546,358

Millan-Gabet, R., Schloerb, F.P., Traub, W.A., Malbet, F., Berger, J.P., & Bregman, J.D. 1999, ApJL, 513, L131

Prato, L., Greene, T.P., & Simon, M. 2003, ApJ, 584, 853

Ressler, M.E., Werner, M.W., Van Clever, J., & Chou, H.A. 1994, Exp. Astr., 3, 277

Ressler, M.E. & Barsony, M. 2001, AJ, 121, 1098

Ressler, M.E. & Barsony, M. 2003, ApJ, 584, 832

Rydgren, A.E., Strom, S.E., & Strom, K.M. 1976, ApJS, 30, 307

Simon,M., Ghez,A.M., Leinert,Ch., Cassar,L., Chen,W.P., Howell,R.R., Jameson,R.F., Matthews,K., Neugebauer,G., Richichi,A. 1995, ApJ, 443, 625

Skrutskie, M., Dutkevitch, D., Strom, S., Edwards, S., & Strom, K. 1990, AJ, 99, 1187

Strom, K.M., Strom, S.E., Edwards, S., Cabrit, S., & Skrutskie, M.F. AJ, 97, 1451

Strom, K.M., Kepner, J., & Strom, S.E. 1995, ApJ, 438, 813

Struve, O. & Rudkjøbing, M. 1949, ApJ, 109, 92

Vrba, F.J., Strom, K.M.., Strom, S.E.., Grasdalen, G.L. 1975, ApJ, 197, 77

Walter, F.M., Vrba, F.J., Mathieu, R. D., Brown, A., & Myers, P.C. 1994, AJ, 107, 714

Whitney, B.A., Wood, K., Bjorkman, J.E., & Cohen, M. 2003, ApJ, 598, 1079

Wilking, B.A. & Lada, C.J. 1983, ApJ, 274, 698

Wilking, B.A., Lada, C.J., & Young, E.T. 1989, ApJ, 340, 852

Wilking, B.A., Greene, T.P., & Meyer, M.R. 1999, AJ, 117, 469

Wilking, B.A., Bontemps, S., Schuler, R.E., Greene, T.P., & André, Ph. 2001, ApJ, 551, 357

Young, E.T., Lada, C.J., & Wilking, B.A. 1986, ApJ, 304, L45

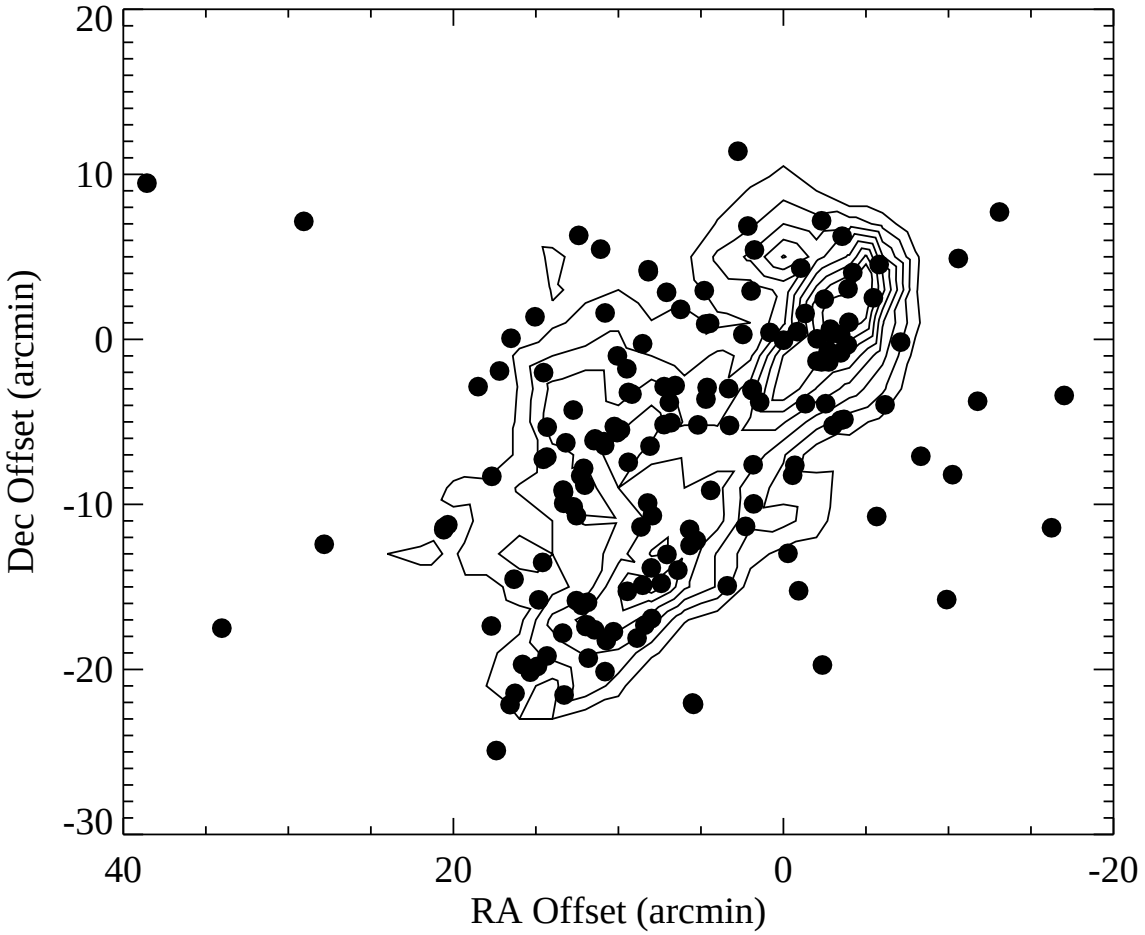

Fig. 1.— The spatial distribution of the target objects for which mid-infrared fluxes and/or flux upper limits are listed in Table 2. The contour plot (courtesy of B. A. Wilking) shows the $C^{18}O$ J=(2→1) integrated intensity in K km/sec units, at 1 K km/sec intervals, starting at 3 K km/sec and ending at 11 K km/sec. The offsets (in arcmin units) are from the (0,0) position of S1: α_{2000} =16h 26m 34.2s, $\delta_{2000} = -24^\circ\ 23'\ 27''$.

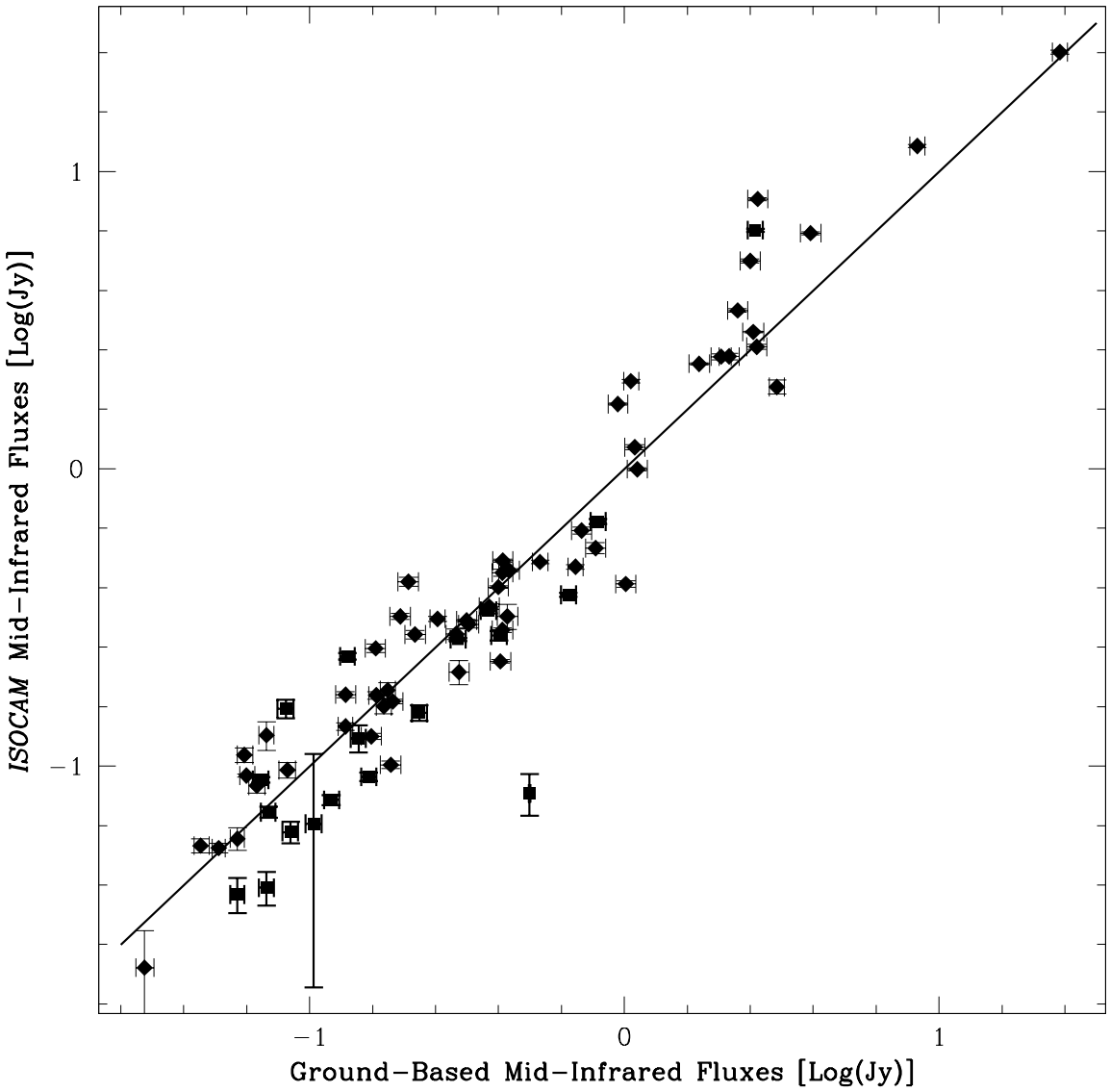

Fig. 2.— Plot of ground-based mid-infrared fluxes for objects in Table 2 vs. mid-infrared fluxes from *ISOCAM*. The 69 objects plotted here were common to, and detected by, both surveys. Furthermore, each object plotted here was detected through both *ISOCAM* filters, centered at 6.7 μm and 14.3 μm, respectively. Filled diamonds represent objects detected by MIRLIN at 10.8 μm, with linearly interpolated *ISOCAM* 10.8 μm fluxes. Filled squares represent objects detected by LWS at 12.5 μm, with linearly interpolated *ISOCAM* 12.5 μm fluxes.

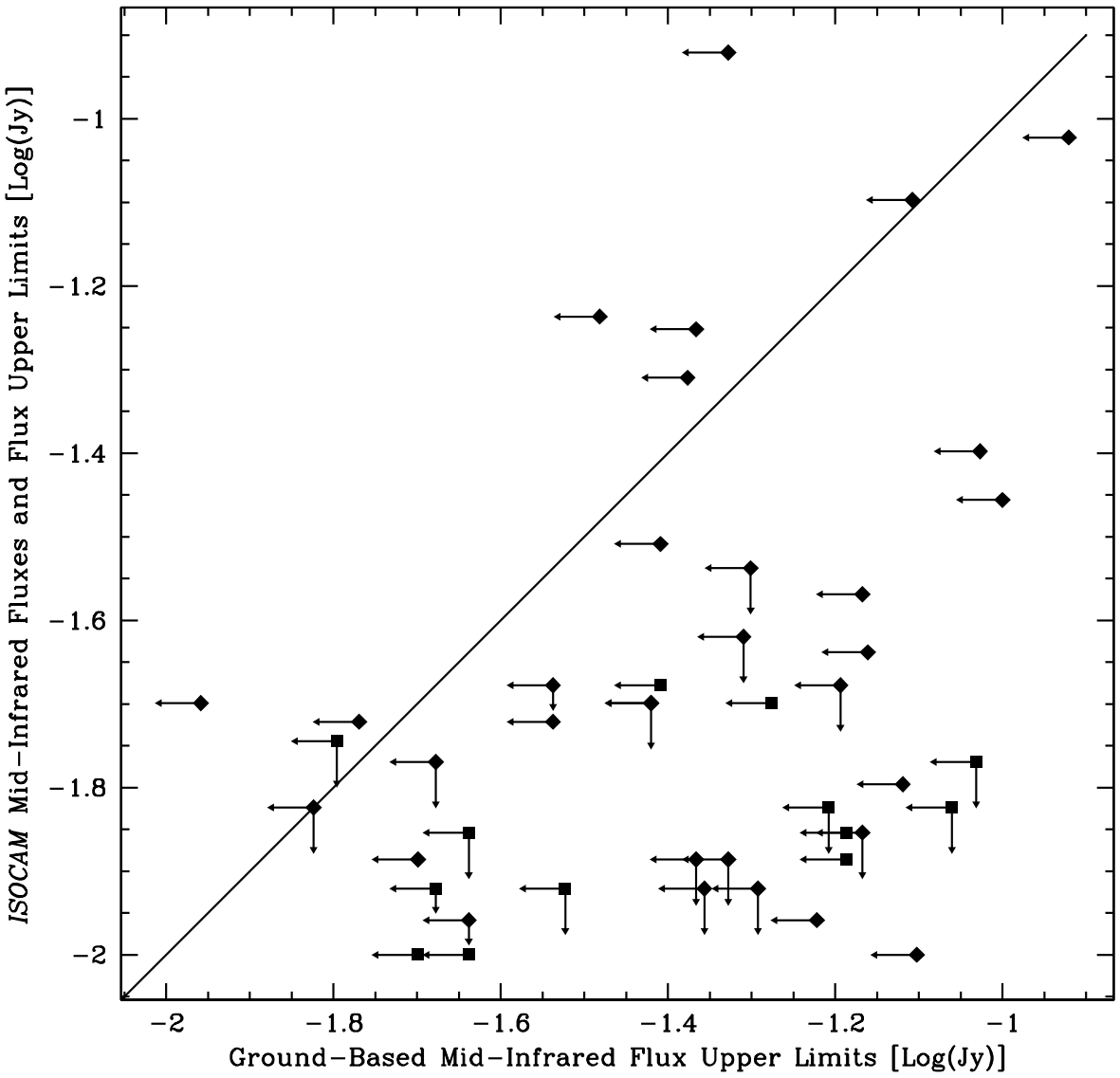

Fig. 3.— Plot of ground-based mid-infrared flux upper limits for objects in Table 2 in common with *ISOCAM*-detected objects. Filled diamonds represent MIRLIN 10.8 μm upper limits; filled squares represent LWS 12.5 μm upper limits. *ISOCAM* fluxes were interpolated to 10.8 μm (filled diamonds) or to 12.5 μm (filled squares) for objects detected in both *ISOCAM* filters. For objects detected only at 6.7 μm by *ISOCAM*, the 14.3 μm completeness limit of 15 mJy is used to derive the interpolated *ISOCAM* flux upper limits.

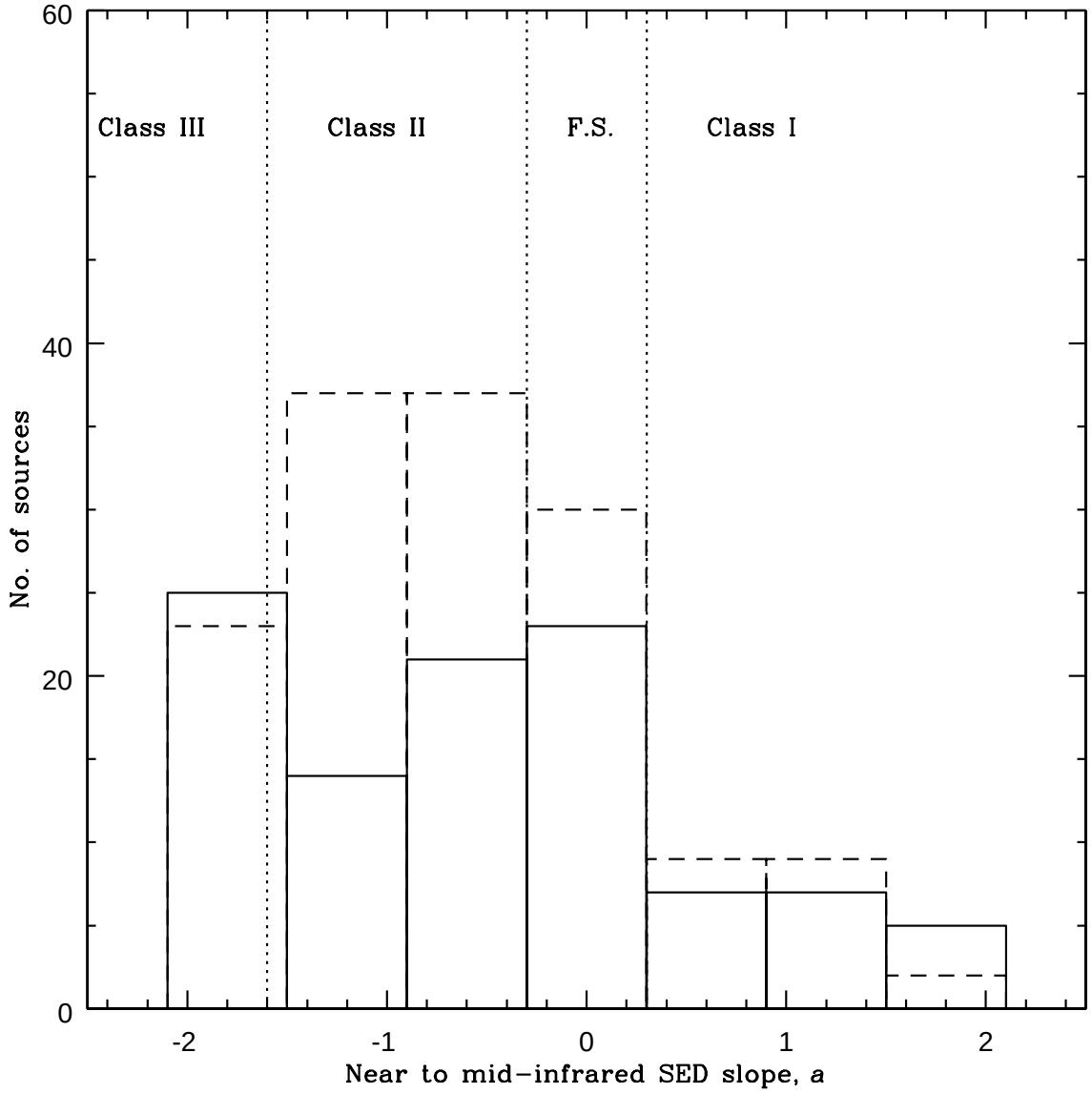

Fig. 4.— Histogram of the *observed* distribution of the near- to mid-infrared spectral slopes of ρ Oph embedded sources: The solid line histogram represents sources with SED slopes, a, determined using mid-infrared data from this work; the dashed line histogram represents SED slopes determined from the 14.3 μm *ISOCAM* photometry. The 2.2 μm photometry of Barsony et al. (1997) was used in both cases. Note the large population of Flat Spectrum ($-0.3 \leq a \leq +0.3$) objects.

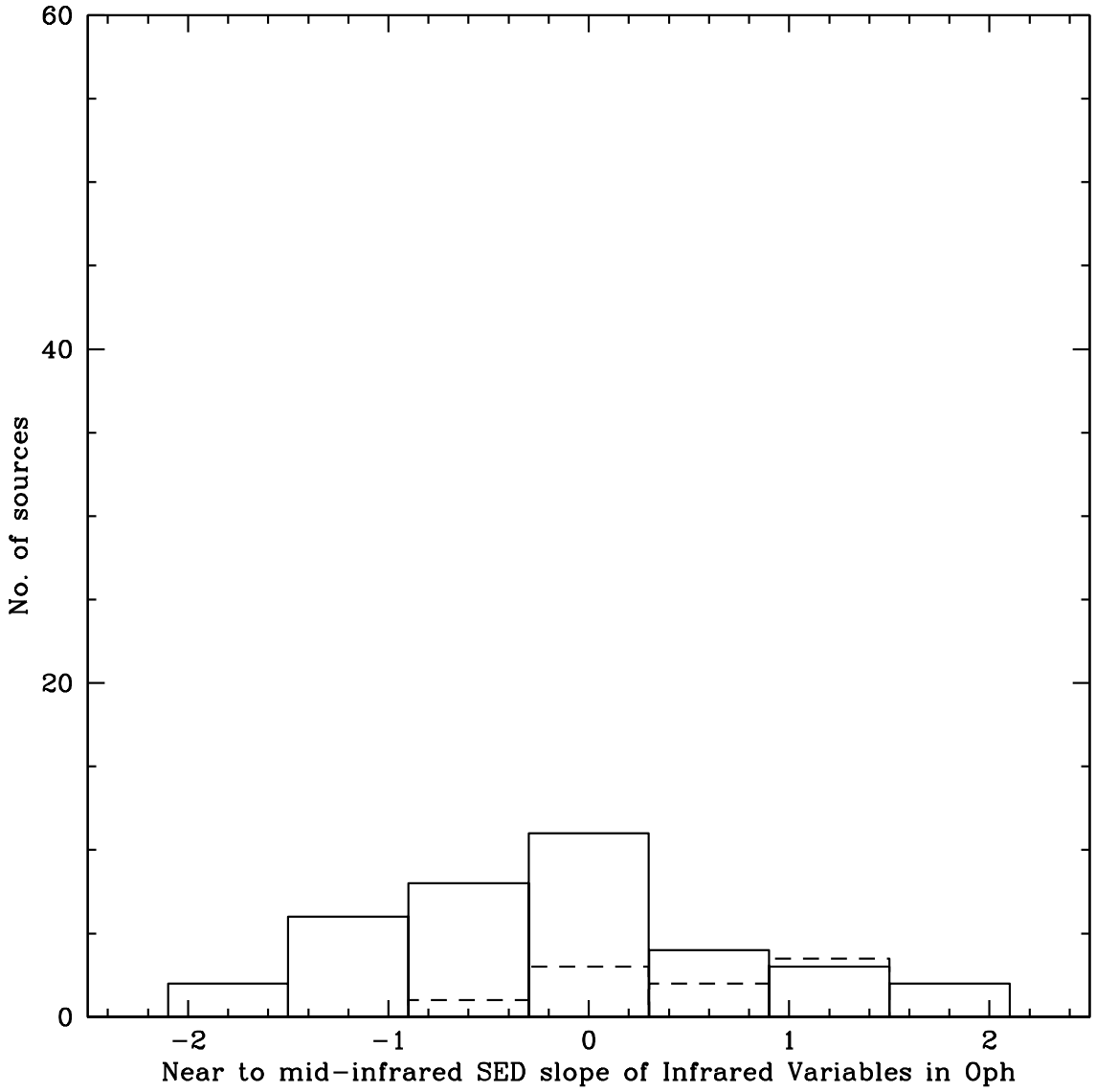

Fig. 5.— Histogram of the *observed* distribution of the near- to mid-infrared spectral slopes of ρ Oph variables: The solid line represents this distribution for the mid-infrared variables of Table 3; the dashed line represents the SED distribution of the near-infrared variables from Table 5 of Barsony et al. (1997). Note the tendency of the NIR variables towards earlier SED classes, whereas the mid-IR variables seem to be evenly distributed through the SED classes with optically thick disks.

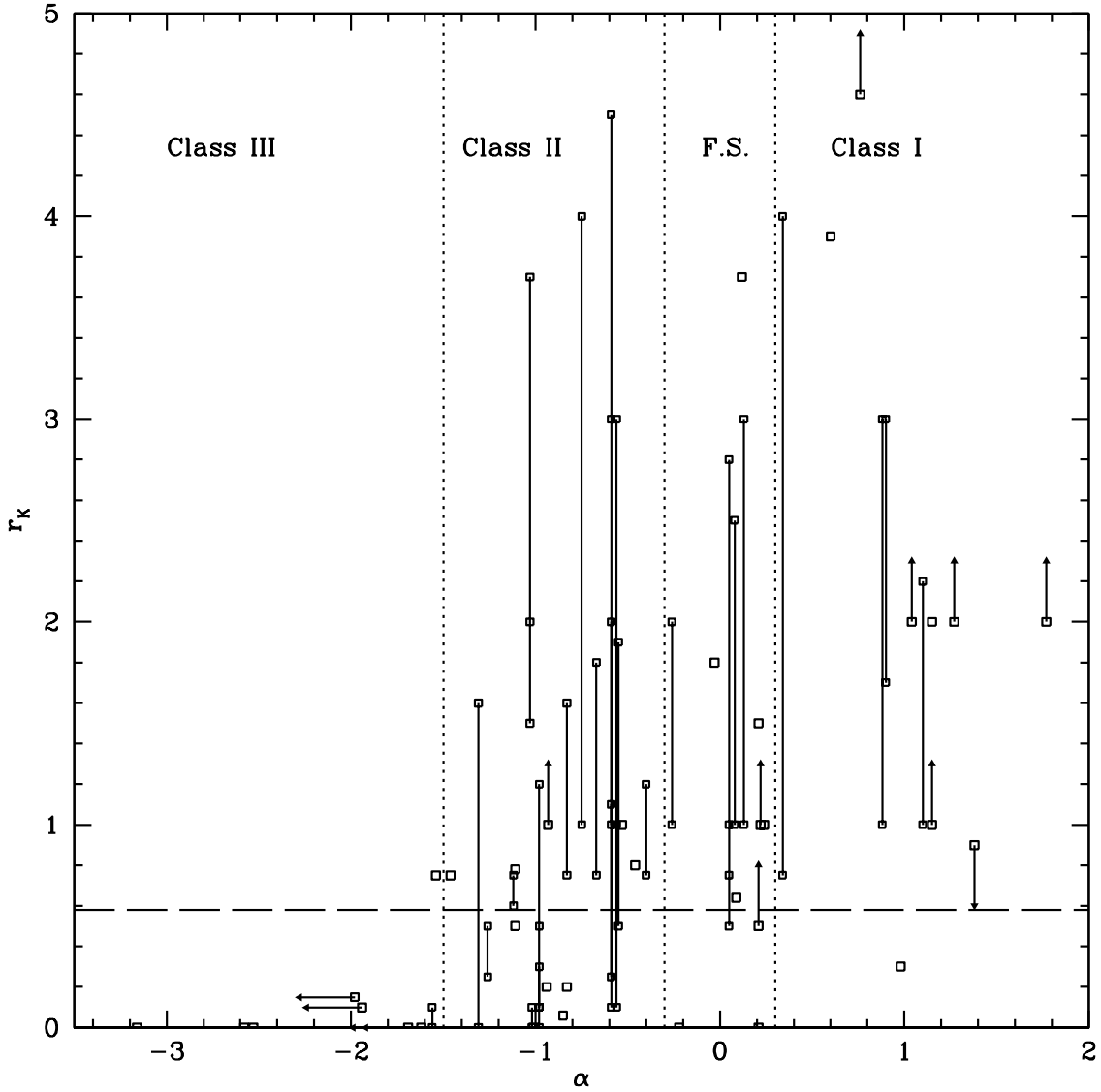

Fig. 6.— Plot of the K-band veiling (r_K values) vs. the SED slopes, α, for ρ Oph embedded sources from Table 4. Note that large variability in K-band veiling is a ubiquitous phenomenon amongst all SED classes with optically thick disks. This is a robust result, withstanding any errors that may have been introduced by the use of non-simultaneous near- and mid-IR photometry in the determination of the plotted SED slopes. The horizontal dashed line, drawn at $r_K = 0.58$ indicates the dividing line between optically thick (above the line) and optically thin (below the line) disks (Wilking et al. 2001).

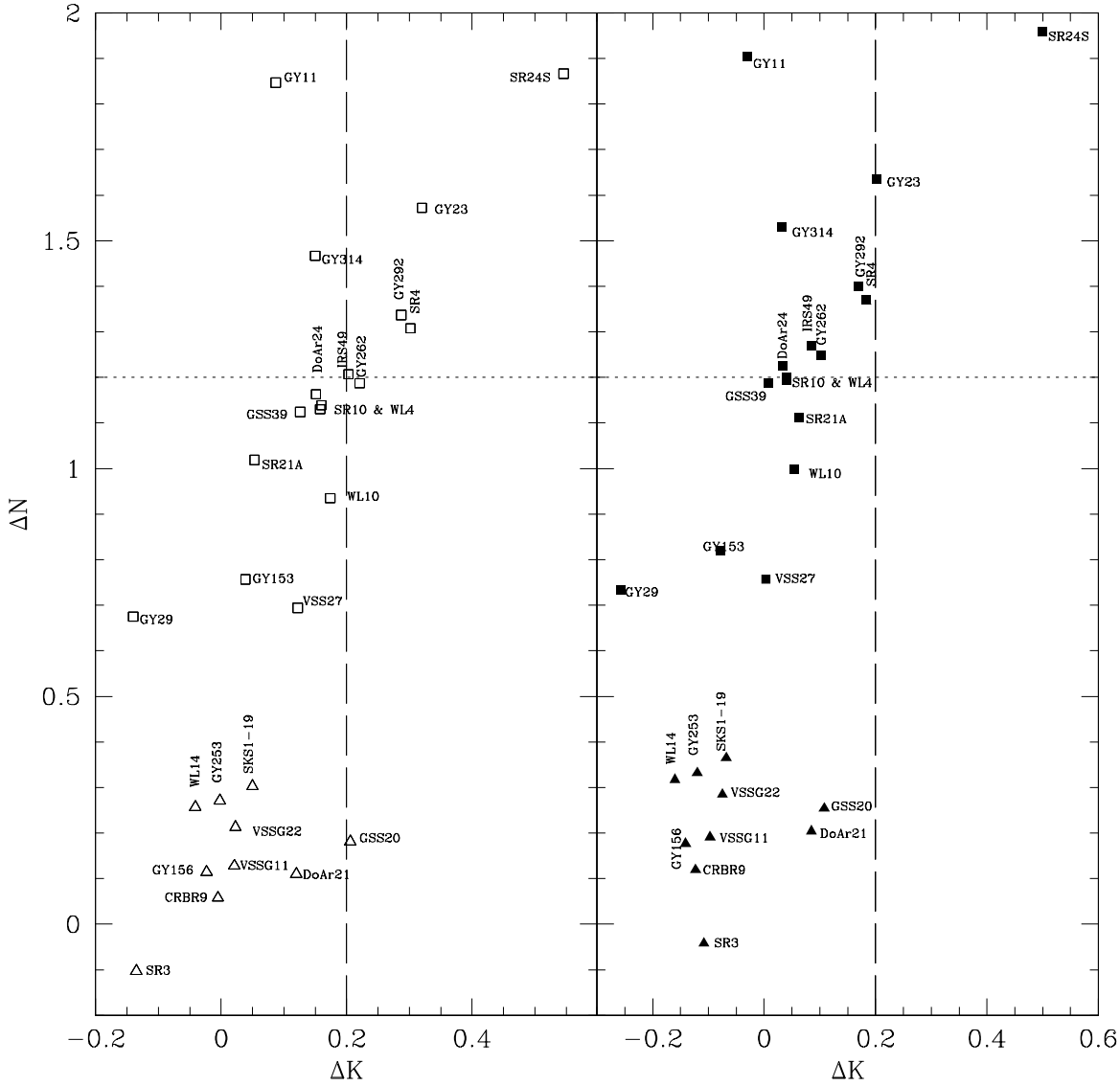

Fig. 7.— Plot of excess emission (above photospheric) at near-infrared (ΔK) and mid-infrared (ΔN) wavelengths for Class II objects (squares) and Class III objects (triangles) for which spectroscopic T_{eff} measurements are available. The vertical dashed line at $\Delta K = 0.2$ indicates the boundary between optically thick ($\Delta K \geq 0.2$) and optically thin ($\Delta K \leq 0.2$) inner disks. The horizontal, dotted line at $\Delta N = 1.2$ indicates the boundary between optically thick ($\Delta N \geq 1.2$) and optically thin ($\Delta N \leq 1.2$) disk regions further out. In the left panel, with open symbols, blackbody emission was used to model the central YSO, whereas in the right panel, with filled symbols, Kurucz model atmospheres of the appropriate effective temperature were used to model the central YSO.